Journal Pre-proof

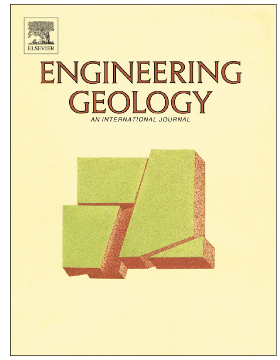

Numerical analysis of the influence of 3D geometry and seismic input on rock-slope failures triggered by moderate to strong earthquakes: An example from the 2016 Central Italy seismic sequence

Luca Schilirò, Luca Smeraglia, Chiara Varone, Giovanni Forte, Paolo Tommasi

PII: S0013-7952(26)00275-9

DOI: https://doi.org/10.1016/j.enggeo.2026.108816

Reference: ENGEO 108816

To appear in: *Engineering Geology*

Received date: 11 October 2025

Revised date: 21 March 2026

Accepted date: 12 May 2026

Please cite this article as: L. Schilirò, L. Smeraglia, C. Varone, et al., Numerical analysis of the influence of 3D geometry and seismic input on rock-slope failures triggered by moderate to strong earthquakes: An example from the 2016 Central Italy seismic sequence, *Engineering Geology* (2024), https://doi.org/10.1016/j.enggeo.2026.108816

Numerical analysis of the influence of 3D geometry and seismic input on rock-slope failures triggered by moderate to strong earthquakes: an example from the 2016 Central Italy seismic sequence

Luca Schilirò [1], Luca Smeraglia [1,2], Chiara Varone [1]*, Giovanni Forte [3], Paolo Tommasi [1]

[1] Istituto di Geologia Ambientale e Geoingegneria del Consiglio Nazionale delle Ricerche (CNR IGAG), Rome, Italy; luca.schiliro@cnr.it; luca.smeraglia@cnr.it; chiara.varone@cnr.it; paolo.tommasi@cnr.it

[2] Chrono- Environnement, Université Marie & Louis Pasteur, Besançon, France

[3] Dipartimento d'Ingegneria Civile, Edile e Ambientale, Università degli Studi di Napoli Federico II, Naples, Italy; giovanni.forte@unina.it

* corresponding author: Chiara Varone (chiara.varone@cnr.it)

Abstract

This study analyzes the Valle Orteccia rock slide, one of the most significant rock slope failures triggered by the 2016 Central Italy seismic sequence. Numerical simulations of the initial stage of the failure were performed in both static and dynamic conditions, using high-resolution geological-structural and geomechanical data derived from UAV (Unmanned Aerial Vehicle) surveys and in-situ investigations. The analysis revealed that the slope reached near-critical conditions during the M_w 5.9 Visso earthquake (26 October 2016) and collapsed in the early stage of the subsequent M_w 6.5 Norcia event (30 October 2016). The failure mechanism was primarily driven by three major discontinuities, in combination with local slope morphology, which enhanced seismic amplification effects in the upper-central part of the slope. This work demonstrates that a 3D modeling approach can be a powerful tool for reconstructing complex slope failure/deformation events controlled by a strongly 3D rock mass structure and directional seismic effects that cannot be adequately considered in simpler analyses. Since the geo-structural setting of Valle Orteccia may be representative of other sectors in the central-northern Apennines and of thrust front areas worldwide, this work may be of general significance for the study of earthquake-induced landslides on a wider scale.

Keywords: rock slope; earthquake; slope stability; numerical modelling; Central Italy

1. Introduction

Rock slope failures are a primary source of risk for human activities and a major contributor to landscape evolution in steep, mountainous regions. Seismic triggering is usually related to strong (Mw ≥ 7) earthquakes (i.e. Gorum et al., 2023, Kocaman et al., 2025), whose destabilizing effects may develop not only near the epicentre but also in the far-field. Although the occurrence of earthquake-triggered rock slope failures mostly depends on magnitude and epicentral distance (e.g., Zou et al., 2022), their location can also be strongly influenced by other factors, such as rock mass structure (Watman et al., 2025). In particular, the effect of joint orientation and spacing with respect to slope orientation can lead to critical slope stability conditions, influencing the failure mechanism (Fan et al., 2019; Azarafza at al., 2021). Moreover, sharp variations in rock fracturing, for instance in proximity to fault zones (e.g., Agliardi et al., 2013), can lead to significant local amplification effects (e.g., Gischig et al., 2015) due to contrasts in shear wave velocity. Amplification may also be induced by morphological features, such as hilltop slopes, ridges, steep cliffs, and sharp spurs (e.g., Havenith et al., 2003; Li et al., 2019). It was also observed that, on steep slopes, amplification effects vary significantly with elevation (e.g., Pignalosa et al., 2022; Verrucci et al., 2023). These morphological and structural/geomechanical conditions not only control the location of rock slope failures during strong earthquakes but also explain the occurrence of relatively large rock slope failures in response to even moderate-to-strong earthquakes (M_w 5 - 6.5). For instance, during the 2016-2017 Central Italy seismic sequence hundreds of landslides were triggered (e.g., Martino et al., 2017; Lanzo et al., 2019; Martino et al., 2019), mostly small rockfalls, but also several major rockslides (e.g., Tommasi et al., 2019; Forte et al., 2021; Schilirò et al., 2024), with a maximum volume of 70,000 m3 for Sasso Pizzuto landslide (Romeo et al., 2017). However, despite the large number of studies on earthquake-induced rock slope failures, most analyses still rely on simplified kinematic approaches or two-dimensional numerical models. While these methods are effective for first-order and rapid post-earthquake assessments, they often fail to capture the combined effects of three-dimensional rock mass structure, complex slope morphology, and directional seismic wave propagation. In this respect, comparative studies (Firincioglu and Ercanoglu, 2021; McQuillan and Bar, 2023) show that 2D approaches may misrepresent failure mechanisms and over-estimate stability conditions when out-of-plane effects and anisotropy are important. Furthermore, the role of intersecting discontinuity sets and localized topographic amplification in controlling the onset of instability-rather than the final failure geometry-remains insufficiently investigated, especially after moderate-to-strong earthquakes.

In this work, we investigate one of the major landslide events occurred after the 2016-2017 Central Italy seismic sequence, i.e., the Valle Orteccia rock slide, which is located in the Sibillini Mountains National Park (Marche Region, Ussita municipality). The rock slide generated a rock avalanche (see classification by Hungr et al. 2014) with a fan shaped debris of 6000 m2 and a maximum runout of 160 metres. The main aim was to reconstruct and understand the initiation mechanism of the rock slide through Finite Element (FEM) numerical analyses in both static and dynamic conditions.

In particular, we performed numerical stress-strain analyses with the specific objectives of (i) assessing the role of rock mass structure, with specific focus on the features of major discontinuities, and (ii) evaluating the influence of three-dimensional slope morphology on the failure mechanism. For the parameterization of the model, we combined data collected in-situ with UAV-derived information, which are increasingly recognized as reliable for rock mass characterization in steep or inaccessible slopes (Salvini et al., 2020; Wang et al., 2022). Thus, by integrating data-constrained rock mass characterization with fully three-dimensional dynamic numerical modelling, this work contributes to the still-limited set of studies that explicitly resolve the interaction between discontinuity networks, 3D topography, and seismic loading during failure initiation (i.e., Atta and Bera, 2025; Wu et al., 2025). Furthermore, the geo-structural setting of Valle Orteccia, characterized by the interaction between inherited tectonic structures, active fault systems, and steep morphologies resulting from long-term uplift and erosion, closely reflects conditions commonly observed in seismically active mountainous regions. In this sense, the geological–structural and morphological factors controlling this event are not site-specific but are representative of a broader class of earthquake-induced slope instabilities documented in orogenic areas that have undergone a comparable morpho-tectonic evolution. Consequently, the results of this study extend beyond the local scale and provide a robust basis for seismic slope stability analysis and hazard assessment in structurally complex mountainous environments.

2. Geological and structural setting of the area

The study area is located in the central-northern sector of Apennines fold-and-thrust belt (Figure 1a). This fold-belt strikes NW-SE and generated since late Oligocene-to-present due to the progressive retreat of the West-dipping subducting Adriatic slab toward the east below the European plate (e.g., Carminati et al., 2010). The structure of the Apennine belt results from the superposition of an early phase of crustal shortening (orogenic compression) and post-orogenic extension. Contractional deformation was mainly accommodated by N-S to NW-SE-striking folds and W-SW-dipping, E-NE-verging thrusts that stacked pre-orogenic successions above syn-orogenic deposits (e.g., Curzi et al., 2024). Pre-orogenic successions consist of Upper Triassic-middle Miocene carbonates, while syn-orogenic successions consist of upper Miocene siliciclastic sandstone, marl, and shale. Post-orogenic, extensional deformation is associated with NW-SE-striking normal faults, which cut across the orogenic structures and are still active, as evidenced by the most recent 2016–2017 Central Italy seismic sequence (e.g., Chiaraluce et al., 2017), that included the M_w 6.0 Amatrice, M_w 5.9 Visso and M_w 6.5 Norcia mainshocks (Porreca et al., 2018). The tectonic activity is also testified by many other $M_w \geq 6.0$ earthquakes occurred in the last 400 years (e.g., Chiarabba et al., 2009). Focusing on the probabilistic assessment of seismic hazard of the study area, the expected horizontal peak ground acceleration (PGA) with 10% probability of exceedance in 50 years on hard ground (Vs_{30} > 800 m/s) ranges between 0.225 and 0.250g (Stucchi et al., 2011).

The studied rock slide detached from the left flank of a small and narrow suspended valley (Valle Orteccia), which is located on top of the southern Sibillini Mountains (Figure 1b), along the outer front of the central-northern Apennines. The Sibillini Mountains are bounded by the NW-SE-striking Sibillini Thrust Front (STF) and by a major NNE-SSW- to N-S-striking lateral ramp of the Olevano-Antrodoco Line (OAL; Pierantoni et al., 2013; Figure 1a). In particular, the event occurred along the subvertical forelimb of the hanging wall anticline of the Mt. Priora thrust (Figure 2a-b), involving a regularly bedded limestone of the *Maiolica fm.*

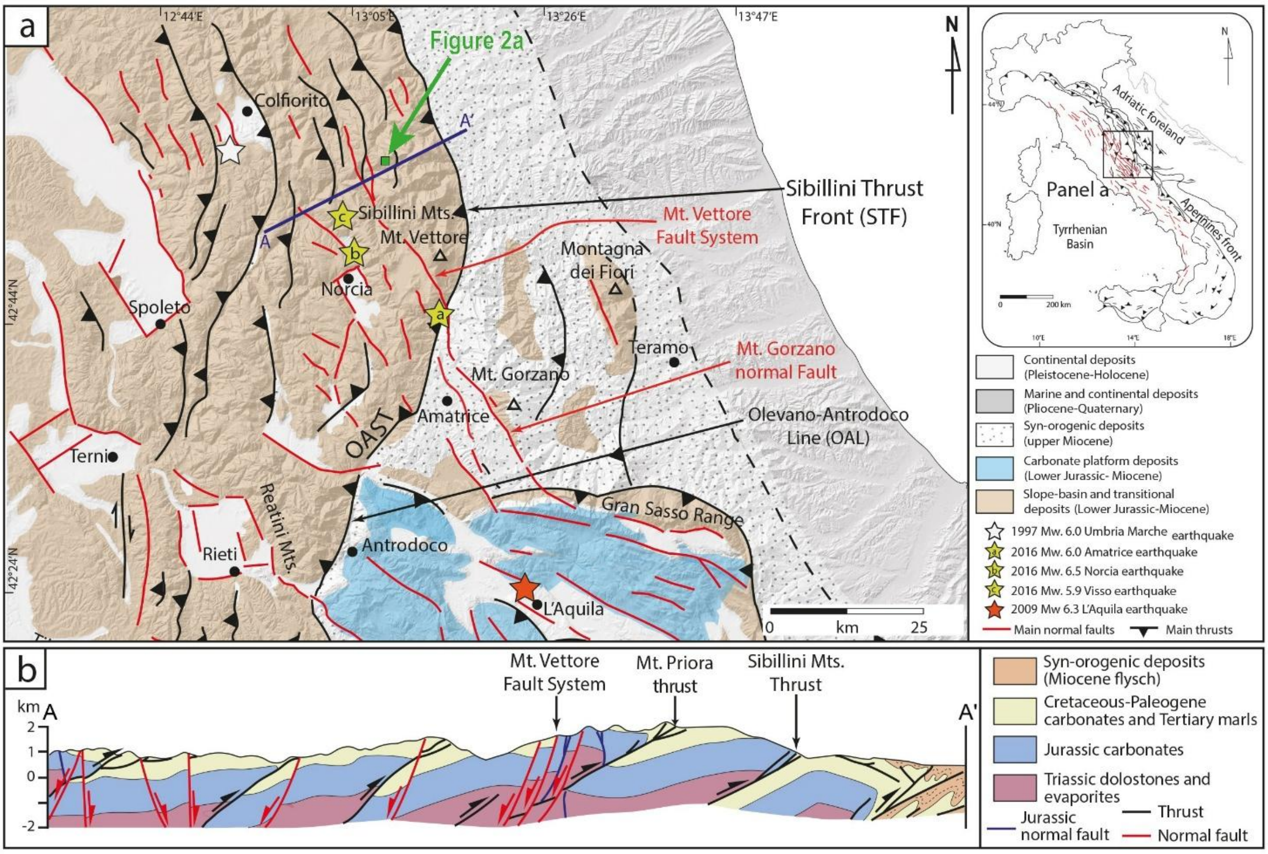

Figure 1: a) simplified geological map of the central-northern Apennines with epicenters of major earthquakes. The location of the study area (green square) is also indicated (see Figure 2a); b) geological cross section across the Sibillini Mountains. Maps and cross sections are modified from Curzi et al., 2024.

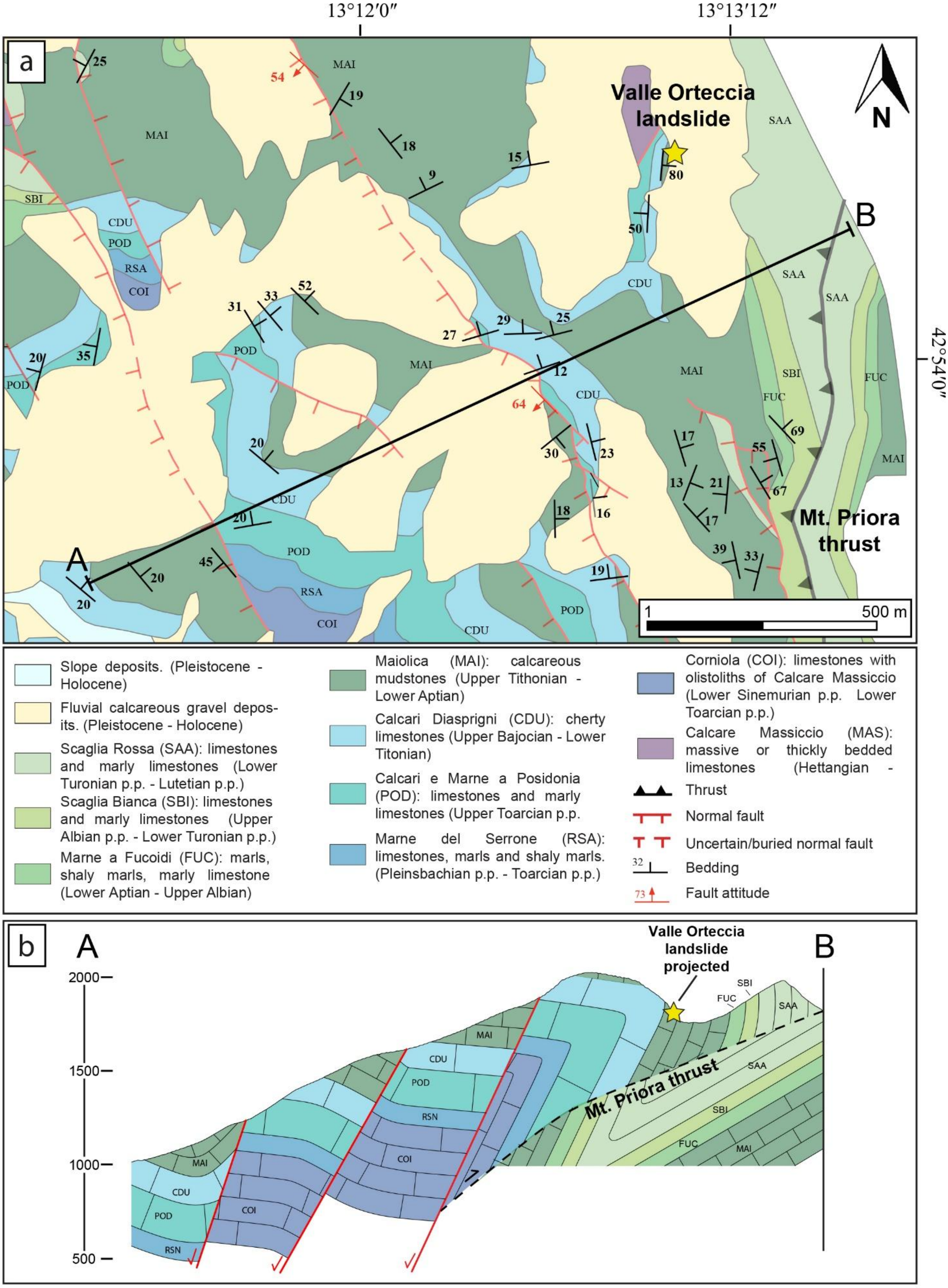

Figure 2: a) detailed geological map of the study area with Valle Orteccia rock slide location; b) geological cross-section across the area affected by the event (from Testa et al., 2019 mod.).

3. Data acquisition and methodology

The geometry of the rock slide was reconstructed through an UAV (Unmanned Aerial Vehicle) photogrammetric survey, from which a detailed VOM (Virtual Outcrop Model) of the investigated slope was produced. The information derived from the VOM were integrated with in-situ geological, structural and geomechanical investigations. Data were used to set up the 3D model for stress-strain analyses in both static and seismic conditions.

3.1. UAV-derived data collection and analysis

The detailed reconstruction of the rock slide scar, as well as the analyses of discontinuity orientation, spacing and surface conditions were performed through a UAV-based aerial 3-D imaging. Images acquisition was primarily captured with a DJI™ Phantom 4 quadrotor UAV platform, equipped with a 1/2.3” CMOS sensor having 94-degree field of view and 12.4 Mpx of effective resolution. UAVs flights covered both the crown and deposition zones and were conducted at an altitude of 70 m above ground level, acquiring both nadir and oblique, with a minimum image overlap of 80% in both flight directions. Captured images were processed using Structure from Motion (SfM) technique, which involves extracting tie points with the Scale-Invariant Feature Transform (SIFT) algorithm (Lowe, 2004) and applying known camera parameters to create a sparse point cloud in a local coordinate system.

The photogrammetric model was georeferenced at this stage using the onboard RTK GNSS system, which provided direct image positioning in a global reference frame. A limited number of ground control points (GCPs) were surveyed exclusively in the deposition zone, where field access was possible and safe, and were used as additional constraints where applicable. To improve the positional accuracy and internal consistency of the reconstruction, a bundle block adjustment (BBA) was performed, refining both camera parameters and sparse point coordinates by minimizing reprojection errors across the image block. Once the camera geometry and the sparse point cloud were fully optimized and georeferenced, a dense point cloud was generated. The latter was cropped to the inaccessible crown area using the open-source software CloudCompare v2.10.2, excluding the GCPs located in the accumulation zone from the final dataset. The resulting point cloud consists of 4,608,998 points over an area of approximately 3,361 m², with an average density of about 1,370 points/m². From this cropped and georeferenced dense cloud, a virtual outcrop model (VOM; Fig. 3a), a 3D meshed surface, a digital surface model (DSM), a digital elevation model (DEM), and a set of high-resolution orthorectified aerial images of the rock slide were generated. The quality of the photogrammetric reconstruction was assessed by evaluating the internal geometric consistency between the dense point cloud, the DSM, and the orthophoto with a ground sampling distance, (GSD) around 14 mm. Key geomorphological features, such as scarp edges, tension cracks, and block boundaries, showed no significant misalignments, confirming the geometric consistency of the dense point cloud. The high spatial resolution, combined with a small ground sampling distance (GSD ≈ 14 mm), provides sufficient detail for characterizing the geometry of the major discontinuities delimiting the rock slide scar, as well as features controlling their mechanical behaviour, including surface waviness (medium-scale roughness) and the presence of rock bridges. The use of high-resolution 3D models for surface roughness characterization has become increasingly common in recent years (e.g., Kim et al., 2013; Salvini et al., 2020); however, the imagery must have a sufficiently small GSD to ensure accurate measurements. In this study, the resulting GSD allowed the extraction of 5 m long profiles along major discontinuities (Fig. 3b), from which the angles of large-scale undulations were measured.

Areas of fresh rupture were also identified on the discontinuity surfaces through detailed inspection of high-resolution orthophotos (Fig. 3c). These areas were interpreted as zones associated with the breakage of rock bridges, i.e. portions where the discontinuity is locally replaced by intact rock. Rock bridges can significantly increase discontinuity shear strength and strongly influence rock slope stability (Elmo et al., 2018). Their extent was mapped and measured using CloudCompare and subsequently used to quantify their contribution to shear strength, which was then incorporated into the 3D numerical simulations.

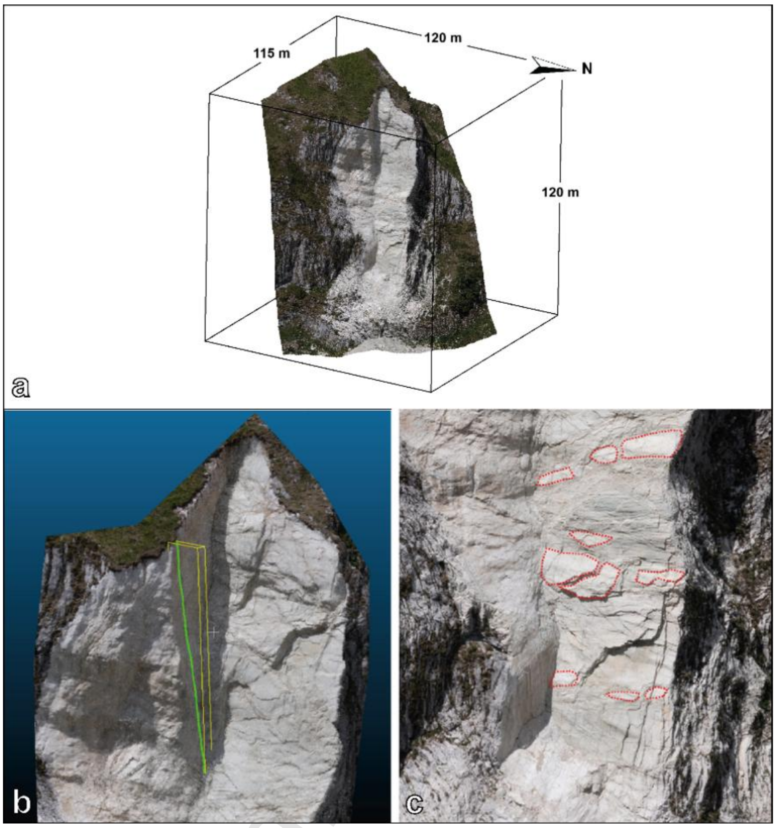

Figure 3: a) VOM of the Valle Orteccia landslide scar, as resulted from the UAV photogrammetric survey; b) example of large-scale roughness profile (green line), as resulted from CloudCompare code*; c) rock bridges' areas inferred from the orthophotos.*

3.2. In-situ data collection and analysis

Two types of in-situ activities were performed on site:

a) Field geological investigations and structural surveys at the base of the slope on accessible outcrops: the collected attitude data were used to integrate the information resulting from the interpretation of the VOM. Both field- and UAV-derived information were related to the main structural elements in the region, identified through the analysis of aerial photographs, existing geological maps and indications from previous studies (Testa et al., 2019);

b) Geomechanical measurements on discontinuity surfaces: Schmidt hammer rebound device and 10 cm long profilometer were used for measuring the strength and small-scale roughness, respectively. Due to the limited accessibility to the landslide scar, measurements were performed on intact rock boulders selected within the blocky slide deposit.

Results of uniaxial compression and ultrasonic pulse tests conducted on rock specimens previously collected in neighbouring outcrops (Forte et al., 2021) were also re-apprised.

3.3. 3D numerical modelling

To analyze the Valle Orteccia event, a three-dimensional FEM model was set up using the Plaxis 3D code (Bentley Systems Inc, 2022). The rock mass was modelled as an equivalent polar anisotropic continuum to account for the closely spaced and persistent bedding joints where major discontinuities are explicitly modelled as interfaces. This schematization of the rock mass was preferred to that utilized by methods for true discontinuous media, like discrete element or discontinuous deformation analyses. In fact, the aim of the study is to investigate the mechanisms acting at the early stages of the movement, when relative displacements between blocks are still limited. With the adopted schematization, internal elastic and plastic deformations of the rock mass due to the main joint set have been however considered, and the role of the more persistent and weaker discontinuities with their actual geometry in controlling the initial displacements of the failed mass has been explicitly taken into account.

We reconstructed the pre-failure slope morphology by manually adjusting the post-failure contour lines on the basis of a pre-event 1:10,000 topographic map (https://www.regione.marche.it/Regione-Utile/Paesaggio-Territorio-Urbanistica/Cartografia/Repertorio/Cartatecnicanumerica110000 accessed on 26 September 2025), coupled with the interpretation of stereo pairs of aerial photographs acquired in 2004 (kindly provided by Umbria Region). The major discontinuities were included as single planes having the orientation shown in the geo-structural analysis. Orientation was obtained by interpolating points of the discontinuity surface extracted from the point cloud provided by UAV photogrammetry.

The spatial resolution of the model discretization grid can lead to an underestimation of amplitude and an overestimation of both group and phase velocities of the dynamic signal (Semblat and Pecker, 2009). To minimize the numerical error, the size of the grid element Δh was chosen according to the following relationship: Δh = λ/25, where λ is the wavelength. Based on the frequency content of the seismic inputs and a S-wave velocity of the rock mass of 1570 m/s, an element size of 5 m was selected, which ensures accurate modeling up to a frequency of 12 Hz. Compliant boundary conditions were also considered to avoid the presence of anomalous seismic waves originated by reflections at the model boundaries.

3.3.1. Choice of input mechanical parameters of the model

Interfaces reproducing major discontinuities can be modelled in Plaxis 3D only with the MC model, which in turn, is characterized by the shear strength angle, φ'_d, cohesion, c'_d and dilation angle, ψ'_d. Parameters φ'_d and cohesion, c'_d were derived by linearizing the Barton-Bandis (BB) model within the normal stress range acting in situ (e.g., Dai et al., 2022):

$$\tan\varphi'_d = \tan\left[\varphi_b + JRC_n \log_{10}\left(\frac{JCS_n}{\sigma_n}\right)\right] - \frac{\pi\, JRC_n}{180 \ln 10}\left\{\tan^2\left[\varphi_b + JRC_n \log_{10}\left(\frac{JCS_n}{\sigma_n}\right)\right] + 1\right\} \quad (1)$$

$$c'_d = \sigma_n \tan\left[\varphi_b + JRC_n \log_{10}\left(\frac{JCS_n}{\sigma_n}\right)\right] - \sigma_n \tan\varphi'_d \quad (2)$$

$$\psi'_d = \varphi'_d - \varphi_b \qquad with\ \varphi_b = \varphi_r + \omega \quad (3)$$

The BB model considered in this study is a modified version for sliding surfaces, which specifically accounts for both small- and large-scale effects of surface roughness (Bandis, 1990):

$$\tau = \sigma_n \tan\left\{\left[JRC_n \log_{10}\left(\frac{JCS_n}{\sigma_n}\right)\right] + \varphi_r + \omega\right\} \quad (4)$$

where τ represents the shear strength, while σ_n is the normal stress applied to the discontinuity surface. The term φ_r is the residual friction angle, which is assumed to be 31° for this specific rock type (Forte et al., 2021). ω is the average inclination intermediate-scale undulations (~5% of the surface length) along the sliding direction (Bandis, 1990), as measured on 5-m-long roughness profiles obtained from the point cloud data. JCS_n and JRC_n refer to, respectively, the scale-adjusted Joint Compressive Strength and Joint Roughness Coefficient, and are calculated with the following equations (Barton and Bandis, 1982):

$$JCS_n = JCS_0 \left(\frac{L_n}{L_0}\right)^{-0.03\ JRC_0} \quad (5)$$

$$JRC_n = JRC_0 \left(\frac{L_n}{L_0}\right)^{-0.02\ JRC_0} \quad (6)$$

JCS_0 and JRC_0 were derived from in-situ geomechanical measurements, while L_0 is the length of the employed profilometer (100 mm), with L_n representing the reference discontinuity length at large scale (5 m). JCS_0 was calculated using the following empirical correlation:

$$JCS_0 = 2.63\ e^{0.061\ R_L} \quad (7)$$

where R_L is the rebound height adjusted for the actual hammer inclination. This relationship derives from numerous UCS vs. R_L measurements performed on specimens to different carbonate lithotypes of the Umbria–Marche sequence (Forte et al., 2021).

For accounting for the contribution of rock bridges to shear strength of major discontinuities, a total cohesion (c'_{tot}) was estimated according to the simplified approach proposed by Jennings (1970):

$$c'_{tot} = Kc'_d + (1-K)c'_{rb} \quad (8)$$

where c'_{rb} is the cohesion of the material forming the rock bridge, and K is a continuity coefficient which expresses the ratio of the total area of the rock bridges to that of the entire failure surface (A_{tot}):

$$K = \frac{A_{joint}}{A_{joint} + \sum A_{rb}} \quad \text{with} \quad A_{tot} = A_{joint} + \sum A_{rb} \quad (9)$$

where A_{rb} is the area of each rock bridge, while A_{joint} is the joint surface area.

Finally, shear stiffness (K_s) was calculated according to Barton and Bandis (1982) as:

$$K_s = \frac{\sigma_n \tan\left[\varphi_b + JRC_n \log_{10}\left(\frac{JCS_n}{\sigma_n}\right)\right]}{\frac{L_n}{500}\left(\frac{JRC_n}{L_n}\right)^{0.33}} \quad (10)$$

while the normal stiffness (K_n) was assumed as 10 times the shear stiffness (Singh and Goel, 2011).

To model the regularly bedded rock mass in Plaxis 3D we adopted the user-defined Iso-JRMC model, which envisages:

- sliding/tensile failure along “virtual” ubiquitous parallel planes with assigned attitude, representing the joints of a set, necessarily weaker than the surrounding rock;
- development of plastic strains in the rock mass (not along pre-existing discontinuities), whenever limit shear or tensile stresses are reached (Stelzer, 2015).

Each “weak” joint set (for a maximum of three) is characterized by a Mohr-Coulomb (MC) failure criterion with cohesion, shear strength angle, tensile strength and dilation angle (c'_j, φ'_j, σ_{tj} and ψ'_j, respectively). In the here considered model, bedding was the only “weak” joint set, thus depicting the shear strength similarly to the Jaeger’s criterion (Jaeger, 1960). The parameters of this joint set were assigned using the same criteria described for the major joint J2.

The bedding bounded rock mass is characterized by MC criterion parameters (cohesion c', friction angle φ', tensile strength σ_t, and dilation angle ψ) which account for the strength contribution of the rock material and of all joints not belonging to the weak set(s).

The parameters of the MC criterion for the bedding bounded rock mass can be conveniently derived by the Hoek and Brown criterion (HB), which depicts strength also at low confining stress (Kumar et al., 2019), whose generalized form is (Hoek et al., 2002):

$$\sigma_1 = \sigma_3 + \sigma_{ci}\left(m_b \frac{\sigma_3}{\sigma_{ci}} + s_b\right)^a \quad (11)$$

where σ_1 and σ_3 are the major and minor effective principal stresses, σ_{ci} is the uniaxial compressive strength of the bedding bounded rock mass, while m_b, s_b and a are parameters related to rock mass structure, depending on the Geological Strength Index (GSI), and the degree of loosening expressed by the disturbance factor (D). Therefore, we assigned to φ' and c' of the Iso-JRMC model the friction angle and cohesion from linearization of the HB criterion proposed by Hoek et al. (2002), and furtherly adjusted (as regards eq. 16) by Li et al. (2008) within the range of confining stresses acting in our slope:

$$\varphi' = \sin^{-1}\left[\frac{6am_b(s_b+m_b\sigma'_{3n})^{a-1}}{2(1+a)(1+2a)6am_b(s_b+m_b\sigma'_{3n})^{a-1}}\right] \quad (12)$$

$$c' = \frac{\sigma_{ci}[(1+2a)s+(1-a)m_b\sigma'_{3n}](s_b+m_b\sigma'_{3n})^{a-1}}{(1+a)(1+2a)\sqrt{1+\frac{6am_b(s_b+m_b\sigma'_{3n})^{a-1}}{(1+a)(1+2a)}}} \quad (13)$$

$$\sigma'_{3n} = \frac{\sigma'_{3\,max}}{\sigma_{ci}} \quad (14)$$

$$\sigma'_{cm} = \sigma_{ci}\frac{[m_b+4s_b-a(m_b-8s_b)]\left(\frac{m_b}{4}+s_b\right)^{a-1}}{2(1+a)(2+a)} \quad (15)$$

$$\frac{\sigma'_{3\,max}}{\sigma'_{cm}} = b\left(\frac{\sigma'_{cm}}{\gamma H}\right)^p \quad (16)$$

where $\sigma'_{3\,max}$ is the maximum confining pressure, γ is the unit weight and H is the average depth of the mobilized material (20 m). b was set equal to 0.2 and p to -1.07 for a slope angle ≥ 45°. Considering the good quality of the bedding bounded rock mass rock mass, ψ' was assumed equal to $\varphi'/6$ (Hoek and Brown, 1997), while σ_t was calculated as:

$$\sigma_t = c' \cot \varphi' \tag{17}$$

Finally, the elasticity modulus *E* was calculated according to the equation proposed by Hoek et al. (2002):

$$E(GPa) = \left(1 - \frac{D}{2}\right) \sqrt{\frac{\sigma_{ci}}{100}}\ 10^{[(GSI-10)/40]} \tag{18}$$

and the shear modulus (G) calculated from *E* assuming a Poisson's ratio equal to 0.3.
GSI was derived from RMR_{89}, calculated with mean spacing measured on the point cloud and with joint condition parameters from in situ surveys.

3.3.2. Numerical analyses

Both static and dynamic analyses were performed. In the former, the factor of safety (FS) was determined using the Strength Reduction Method (SRM) (e.g., Lin et al., 2020), which consists in a progressive reduction of the material strength parameters (friction angle, φ' and cohesion, c') by successive increments ΔFS, until the lowest shear strength value able to maintain the slope stability is reached. FS is then calculated according to:

$$FS = \sum \Delta FS = \frac{\tan \varphi'_{input}}{\tan \varphi'_{reduced}} = \frac{c'_{input}}{c'_{reduced}} \tag{19}$$

where φ'_{input} and c'_{input} are, respectively, the friction angle and cohesion of the material given as input data, while $\varphi'_{reduced}$ and $c'_{reduced}$ are the corresponding reduced values.

The dynamic analyses were performed considering two main events of the 2016 Central Italy seismic sequence, i.e., the Visso (26 October 2016, M_w 5.9) and Norcia (30 October 2016, M_w 6.5) earthquakes (Table 1). We used accelerograms recorded by the temporary seismometric station installed by INGV (National Institute of Geophysics and Volcanology) in the municipality of Castelsantangelo sul Nera (station code CNE; elevation: 798 m a.s.l.), which is the closest seismic station to the Valle Orteccia rock slide. Since this station is located on a soil of class C according to the Eurocode 8 (EC8) classification (CEN, 2004), local seismic site effects could not be excluded. The signals at bedrock depth (25 m below station ground level, i.e., 773 m a.s.l.) were then obtained through numerical simulation, based on the seismic stratigraphy defined in the Level III microzonation study of the area (https://www.webms.it/, accessed September 2025). These accelerograms were then used as input motions for a 1D equivalent-linear numerical modeling to retrieve the seismic records at the seismic bedrock at the slope base (elevation: 1573 m a.s.l.). For each record, the significant duration, i.e., the time required to accumulate between 5% and 95% of the total Arias intensity (Dobry and Idriss, 1978) was considered to define the input motion for the 3D numerical analyses of the Valle Orteccia slope stability (Figure 4).

Table 1: main characteristics of Visso and Norcia earthquakes.

Event			*Seismic station*	*Epicentral distance*	*Horizontal E-W PGA*	*Horizontal N-S PGA*	*Vertical PGA*
Epicenter	*Date*	*Mw*	*ID*	*km*	*m s^{-2}*	*m s^{-2}*	*m s^{-2}*
Visso	26/10/2016	5.9	CNE	2	5.27	3.73	3.89
Norcia	30/10/2016	6.5	CNE	6.7	4.66	2.88	5.36

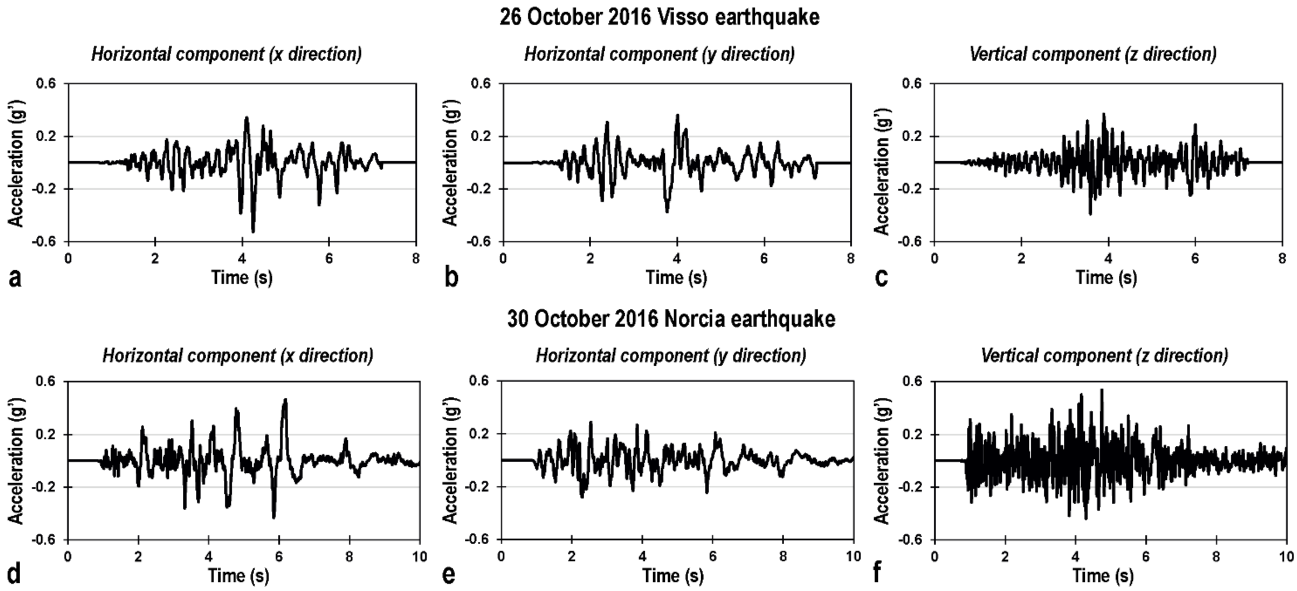

Figure 4: accelerograms of the horizontal and vertical components of 26 October 2016 Visso earthquake (a-c); 30 October 2016 Norcia earthquake (d-f).

4. Results

4.1. Geometry of the rock slide and structural analysis of the slope

The Valle Orteccia rock slide involved an estimated volume of approximately 20,000 m^3, formed by limestones of *Maiolica fm*, which are subdivided into regular subvertical thinly bedded layers (0.1- to 0.5 m-thick), by bedding joints, at times with a thin stiff clay infilling (few millimeters). Clay-filled joints have been frequently found in the Maiolica fm. (Graziani et al., 2009; Pierantoni et al., 2013). The failed rock mass had the shape of a very slender prism whose height, width and thickness were 90 m, 20 m and 20 m, respectively. The rock slide deposit is highly fragmented, with maximum size of the boulders not exceeding 1.5 metres (Fig. 6c). This represents the higher source of direct risk because a trail of the national park of Sibillini Mt.s winds at the foot of the slope. Actually, a rockslide of larger volume could dam the valley and form a small landslide lake. In case of dam failure, the valley below, which host touristic trails and livestock rearing, could be inundated.

The structural measurements showed that the bedding joints dip steeply (60°-80°) towards E-ENE (Figure 5 a-c). Few, meso-scale asymmetric parasitic folds (both anticlines and synclines) are also present (Figure 5d), with sub-horizontal, N-S to NNW-trending fold axis. These folds provide gentle undulations along bedding joints. We also noticed the presence of a large, subvertical WNW-striking strike slip fault with an undulated surface featured by sub-horizontal striation and grooves. (Figure 5e). In the light of this analysis, the failed volume is delimited by three major discontinuities (Figure 6a):

- a subvertical joint J1 (acting as lateral release surface);
- a steeply dipping and gently undulated persistent bedding joint (or combination of few bedding joints) (J2),
- a WNW-striking strike-slip fault (J3).

Following the classification proposed by Hungr et al. (2014), these features suggest that the Valle Orteccia rock slide should be classified as a compound rock slide, rather than a rock wedge slide.
The three major discontinuities are also clearly identifiable in the numerous large blocks contained within the landslide deposit. Specifically, the bedding joints (i.e., associated with set J2) can be

recognized because they are frequently stylolithic and/or contain a thin, hard clay infilling adhering to the joint surface. Fault-related discontinuities (i.e., associated with set J3) are identified by the presence of striations or slickensides, which are typical indicators of shear displacement along fault-related surfaces. Finally, discontinuities belonging to the third joint set (i.e., J1) were recognized based on their orientation with respect to the other two sets.

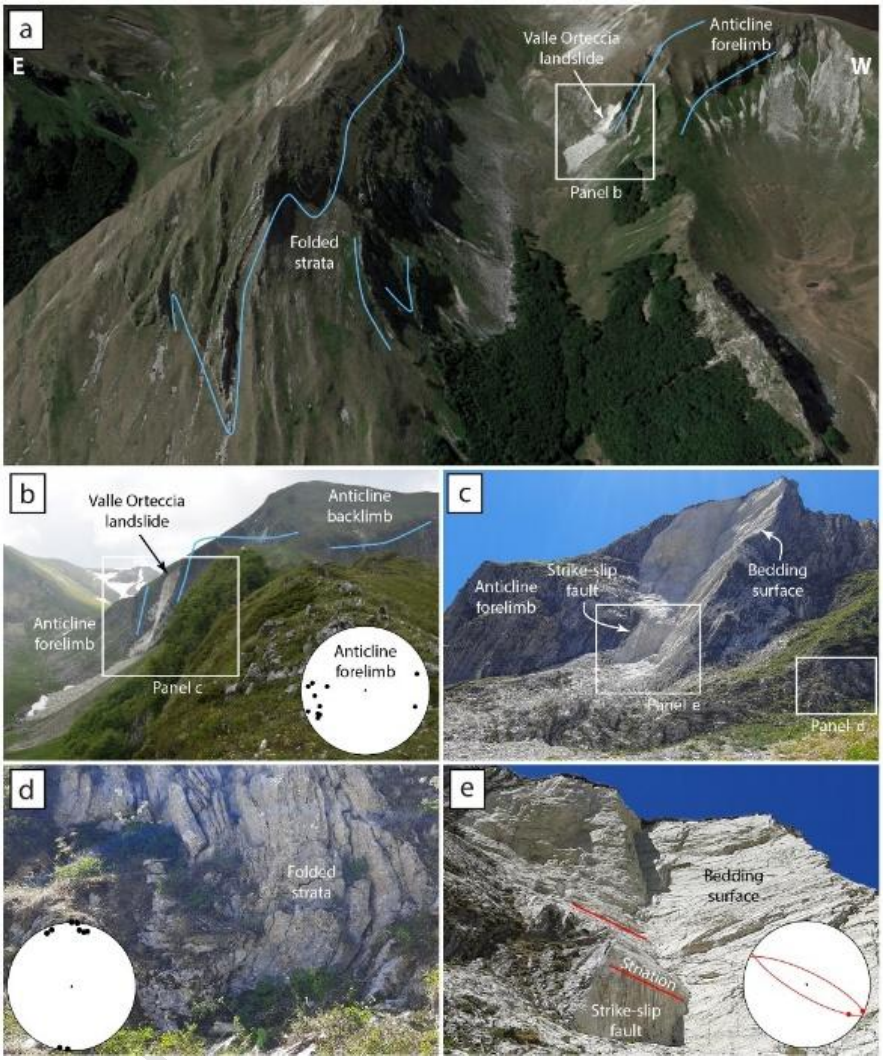

Figure 5: a) Google Maps bird's-eye view of the Valle Orteccia area with lines of maximum bedding dip. The subvertical strata of the anticline forelimb affected by the rock slide and the folded strata to the East of the event are apparent; b-c) anticline hinge with the subvertical forelimb affected by the rock slide; d) folded strata with subvertical limbs and sub-horizontal N-S-trending fold axis; e) detail of the subvertical forelimb affected by the rock slide.

4.2 Reconstruction of the failed mass

A preliminary, simplified kinematic analysis, conducted to assess whether pairs of the three major joints delimiting the failed rock mass could form slender wedges prone to sliding. The analysis reveals that the intersection lines of the three joint pairs (Figure 6b) do not crop out on the slope face, thus avoiding sliding, particularly those which involve bedding. Similarly, planar sliding along the bedding appears unlike, as its dip is equal or higher than that of the slope face. These results help to explain the absence of significant signs of past failures and suggest that a more complex mechanism was responsible for the 2016 failure.

4.3 Numerical analyses

4.3.1 Mechanical and structural parameters adopted in the analyses

The mechanical parameters of the three discontinuity surfaces (Table 2) and those of the rock mass (Table 3) were determined following the approach described in section 3.3.1 and were used for the model interfaces in both static and dynamic configuration. As for the geomechanical parameters of the bedding joints, those referring to the J2 surface were used. The numerical analyses were performed using the same set of geomechanical parameters for both seismic events, within an elastic–perfectly plastic constitutive framework, without incorporating strain softening, hardening, stiffness degradation, or damage evolution.

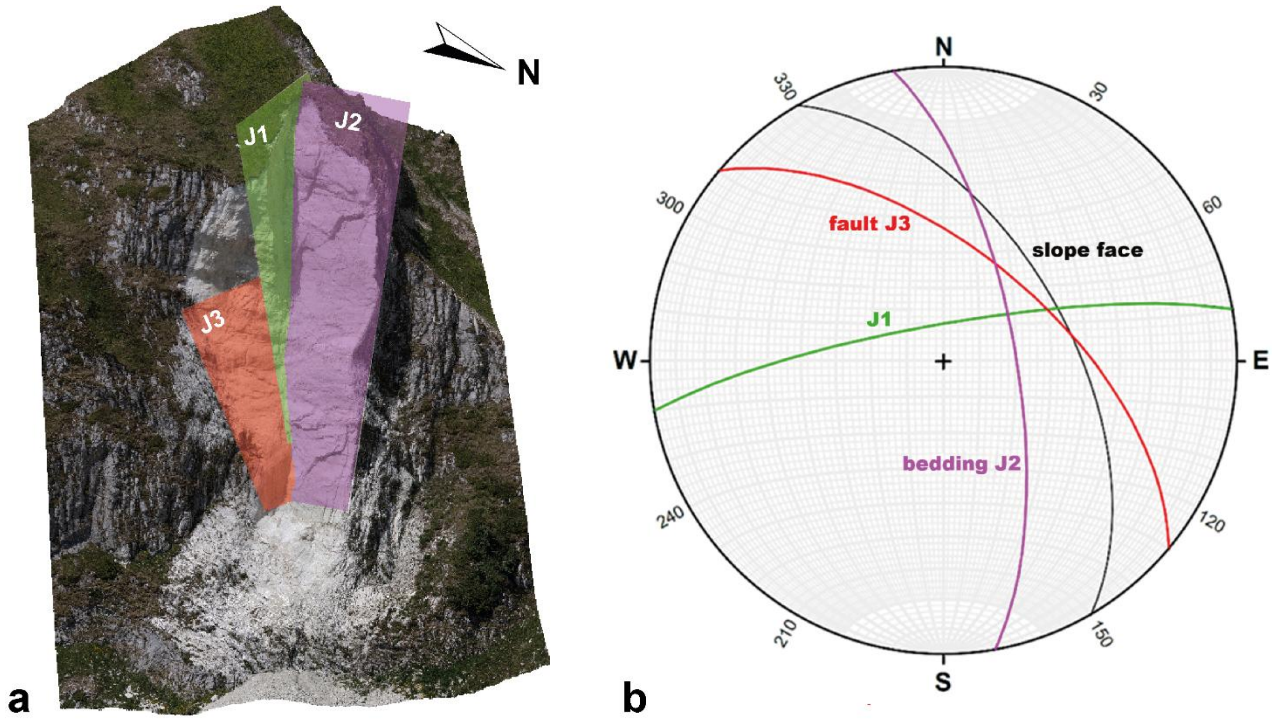

Figure 6: The three major discontinuities resulting from the analysis of the landslide scar (a) and plot of their great circles on the equal-area equatorial stereonet (b) together with the average slope face.

Table 2: Mechanical properties of major discontinuities.

MAJOR DISCONTINUITIES				
Parameter	*Unit*	*J1 value*	*J2 value*	*J3 Value*
Large-scale undulation (ω)	deg.	6	6	8
Joint Compressive Strength (JCS_0)	MPa	43.6	43.6	43.6
Joint Roughness Coefficient (JRC_0)	-	7.3	7.3	7.3
Large-scale Joint Compressive Strength (JCS_n)	MPa	18.5	18.5	18.5
Large-scale Joint Roughness Coefficient (JRC_n)	-	4.1	4.1	4.1
Friction angle (φ'_d)	deg.	45.1	43.5	42.9
Cohesion (c'_d)	kPa	4.9	11.3	16.3

Total cohesion (c'_{tot})	kPa	4.9	85.7	86.3
Dilation angle (ψ'_d)	deg.	8.1	6.5	3.9
Tensile strength (σ_{td})	kPa	0.0	0.0	0.0
Shear stiffness (K_s)	MPa/m	13.0	30.0	43.5
Normal stiffness (K_n)	MPa/m	130	300	435

Table 3: Mechanical properties of the bedding bounded rock mass and bedding joints, the latter derived from those estimated for the J2 surface.

	Parameter	Unit	Value
Bedding bounded rock mass	Uniaxial compressive strength (σ_{ci})	MPa	53
	Unit weight (γ)	kN/m^3	26.1
	Geological Strength Index (GSI)	-	75
	D	-	1
	m_b	-	1.34
	Friction angle (φ')	°	49.7
	Cohesion (c')	kPa	1,150
	Dilation angle (ψ')	°	8.3
	Tensile strength (σ_t)	kPa	980
	Elasticity modulus (E)	GPa	15.3
	Shear modulus (G)	GPa	5.9
Bedding joints	Friction angle (φ'_j)	°	43.5
	Cohesion (c'_j)	kPa	85.7
	Dilation angle (ψ'_j)	°	6.5
	Tensile strength (σ_{tj})	kPa	0

4.3.1 Static analyses

An analysis in static conditions was performed for evaluating the pre-earthquake overall stability of the investigated slope. Assuming the mechanical parameters reported in Table 2 and 3, the first plastic points (i.e., points exceeding maximum shear strength) appear on the discontinuity J3 (Figure 7a). By applying a progressive reduction of the strength parameters, it is possible to observe how the plasticization extends along discontinuities J3 and J2 from the central part of the slope (i.e., where the three main discontinuities intersect), towards the upper and lower part (Figure 7b-c). Finally, the overall failure is preceded by a rapid plasticization of J1 (Figure 7d). The computed displacements provide similar indications on the onset of the potential instability. In this respect, it is possible to notice that displacements initially develop in the inner part of the slope and successively propagate to the entire body delimited by the major discontinuities. The resulting FS is equal to 2.45, which is consistent with the good quality of the rock mass observed in the field.

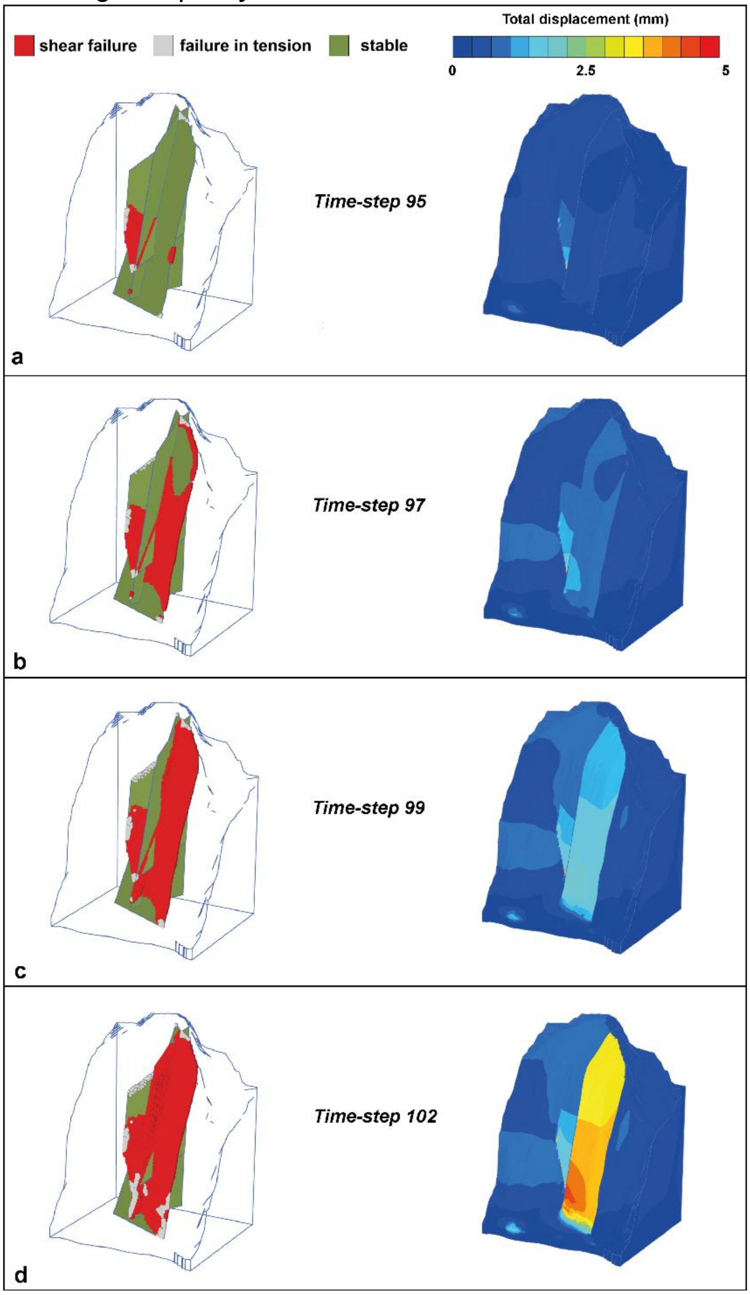

Figure 7: Spatial distribution of shear failure and failure in tension (left column) and total displacement (right column) from the FEM analysis at different time-steps: a) time-step 95; b) time-step 97; c) time-step 99; d) time-step 102 (failure).

4.3.2 Dynamic analyses

The dynamic analyses were conducted to investigate the different response of the Valle Orteccia slope to the 2016 Visso and Norcia earthquakes.

Numerical simulations of the 26 October event show the progressive development of tensile ruptures in the upper part of discontinuity set J1 (Figure 8a-b), followed by tensile ruptures of different portions of the J2 and J3 discontinuity surfaces (Figure 8c-d). These ruptures are associated with total displacements that exceeded 100 mm at the first maximum seismic shaking (approximately 3.5 s) and reached a value of about 230 mm at the end of the event. This displacement pertains to the central-upper part of the slope, where acceleration was approximately twice that recorded at the slope toe (Figure 9a).

However, despite the displacements and tensile ruptures observed during the 26 October event, the slope did not reach a global failure. About 1.6 seconds after the beginning of the 30 October event, there is a further, larger peak of total displacement of almost 250 mm, after which a drop is observed (Figure 9b). At this peak, additional tensile failures appear at the intersection of the three main discontinuities (Figure 10). The detachment of a sector of the rock mass suggests that the rockslide was triggered during the early stages of the Norcia event. This interpretation is consistent with Google Earth imagery acquired between October 27 and 29, which does not show evidence of a significant rock slide in the area following the Visso earthquake.

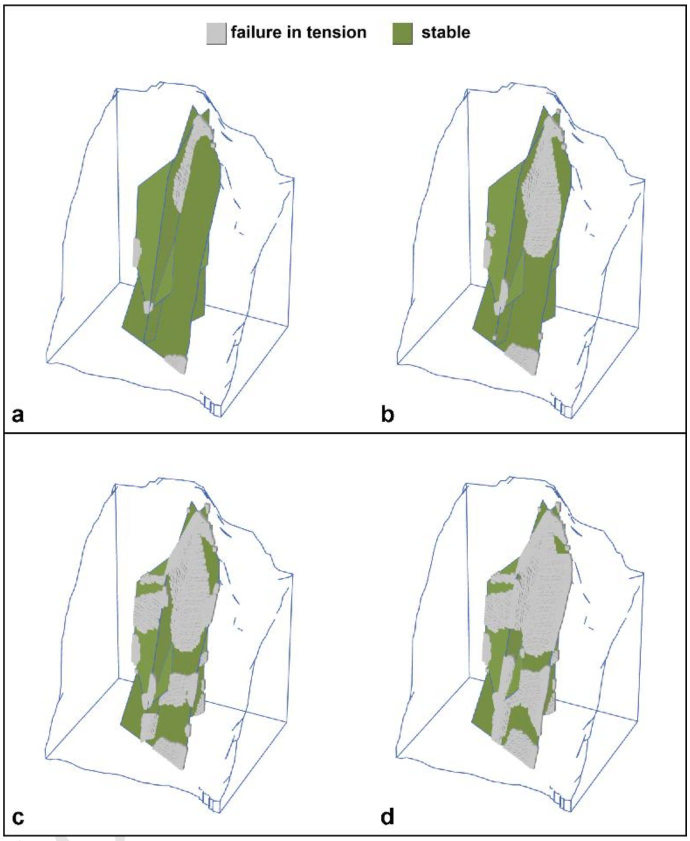

Figure 8: Spatial distribution of points failed in tension from dynamic analysis over successive phases of the 26 October 2016 Visso earthquake: a) 1.500 s; b) 2.000 s; c) 3.750 s; d) 6.700 s.

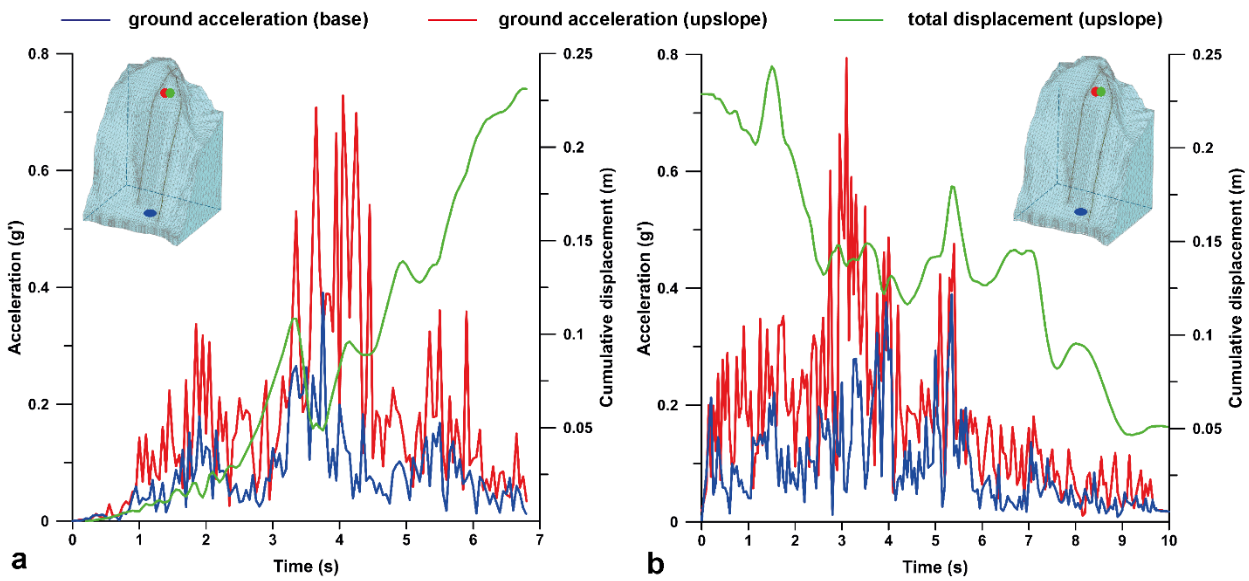

Figure 9: ground acceleration and total displacement calculated at the base and in the central, upper part of the model for (a) 26 October 2016 Visso earthquake and (b) 30 October 2016 Norcia earthquake.

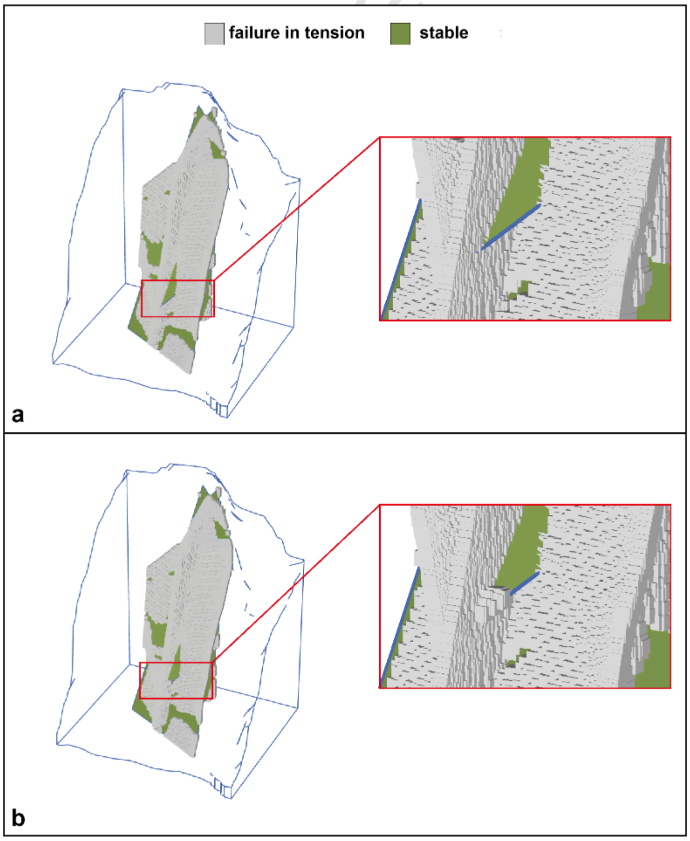

Figure 10: spatial distribution of points failed in tension at (a) 1.650 s and (b) 1.655 s during the 30 October 2016 Norcia earthquake. A detailed view of the intersection zone of the three principal discontinuities is also provided.

The increased displacement observed during both events in the central-upper part of the slope can be attributed to the higher ground accelerations at this elevation, resulting from the steep, pre-failure morphology of the slope. In this context, ground accelerations recorded at two points located adjacent to the collapsed sector in the upper part of the slope were significantly lower than those calculated in the central area (dashed line) for both Visso (Figure 11a) and Norcia (Figure 11b) earthquakes.

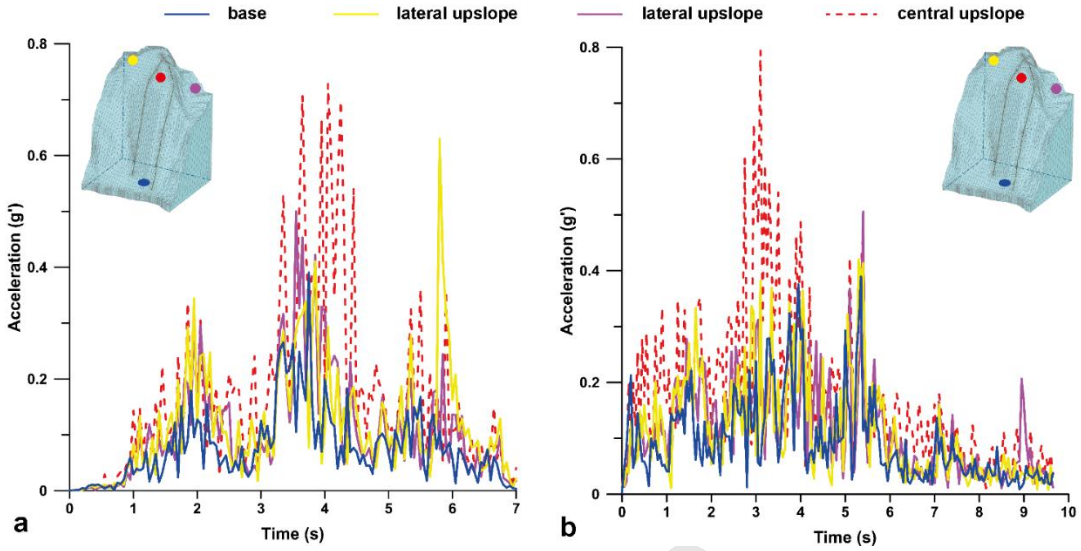

Figure 11: ground acceleration calculated at different points of the slope for (a) 26 October 2016 Visso earthquake and (b) 30 October 2016 Norcia earthquake.

5 Discussions

Numerical modelling suggests some hints on the triggering mechanism of Valle Orteccia event. The stability analysis under static conditions, i.e. before the earthquake, highlighted that, despite the presence of three main discontinuities, the slope was characterized by a high FS (i.e., 2.45). This value depends on the significant strength of both rock mass) and major discontinuities, where the latter is mainly provided by intact rock bridges. To evaluate the significance of specific input parameters related to both rock mass (i.e., GSI and σci) and major discontinuities (i.e., φ'r, JRCn, JCSn and c'tot), a sensitivity analysis was performed. Such an analysis was performed to illustrate how variations in the input parameters affect the initial stability reserve, which in turn influences the outcome of the subsequent dynamic analyses. GSI was varied within the range of 55–80, which encompasses the extreme values derived from field engineering-geological observations. A variability of ±20% was instead applied to σci, as suggested by Ruffolo et Shakoor, 2009.

The shear strength angle φ'_r was reduced from 31°, typical of a rock-to-rock contact for a fresh limestone, to 13° which considers the reduction of shear strength of the asperity surfaces caused by the thin sheared clay infilling of bedding joints. This value of φ'_r is intermediate between the residual shear strength angle determined through direct and ring shear tests on the clay-filled joints of the *Maiolica fm* by Graziani et al. (2009).

A further variation regarded the JRC_n at large displacements. In fact, the BB criterion assumes that, for significant displacements, the contribution of JRC_n is progressively reduced due to the abrasion of the discontinuity surfaces. Therefore, a first scenario was hypothesized ("ultimate strength" *sensu* Krahn and Morgenstern, 1979) in which the JRC_n value (equal to 4.1 see Table 2) is halved, and a second scenario ("residual strength") in which the JRC_n value is assumed equal to zero.

The JCS_n value was varied considering the extreme bounds of the variance of the R_L values obtained from field measurements. This variation (±2) is consistent with the ranges reported by Aydin and

Basu (2005) for slightly weathered rocks. Finally, c'_{tot} was varied considering a maximum and minimum value of the cohesion of the material forming the rock bridge (c'_{rb}, see eq. 17) assuming, respectively, a GSI value equal to 80 and 55.

The analyses indicate that the GSI (i.e., the parameter controlling the strength of the rock mass along planes other than bedding) induces the largest FS variations (Table 4). However, it is important to emphasize that the use of such extreme values for the analysis of the events of 26 and 30 October would produce results that are not consistent with the actual events. In fact, if GSI = 80 were adopted, complete stability would be obtained for both events, while with GSI = 55, the overall failure would already occur during the 26 October event. Considering the GSI range of 80–55 for the calculation of the corresponding C'_{tot} values (126 kPa and 27.2 kPa respectively) leads to the same, inconsistent results for both events.

As regards φ'_r, it can be observed that the value of 13° is probably too low since, also in this case, failure would occur during the first seismic event. Conversely, the JRC_n reduction from ultimate to residual strength has a negligible effect on FS. This can be explained by the low JRC_n value, which reflects the relatively smooth nature of the surfaces of both the bedding planes and the major discontinuity J2. In any case, the sensitivity analysis demonstrated that even with the lowest values, FS remains almost always above 2. This outcome can be explained because the rock bridges have a much higher control on the shear strength, than roughness of the discontinuity surfaces.

Table 4: results of sensitivity analysis for different parameters. The FS variation was calculated considering the reference FS value obtained in static conditions (2.45).

	Parameter	Unit	Value	Static FS	Δ FS (%)	Stability condition after earthquake	
						26 Oct.	30 Oct.
Bedding bounded rock mass	GSI	-	80	2.9	18.4	Stable	Stable
			55	1.7	-30.6	Failure	-
	σ_{ci}	MPa	63.6	2.65	8.2	Stable	Failure
			42.4	2.25	-8.2	Stable	Failure
Major discontinuity	φ_r ; JRC_n	° ; -	31; 2.05	2.3	-6.1	Stable	Failure
			31; 0	2.2	-10.2	Stable	Failure
			13; 2.05	2.1	-14.3	Failure	-
			13; 0	2	-18.4	Failure	-
	JCS_n	MPa	20.9	2.47	0.8	Stable	Failure
			16.4	2.44	-0.4	Stable	Failure
	c'_{tot}	kPa	126	2.75	12.2	Stable	Stable
			27.2	2.1	-14.3	Failure	-

Continuity, small spacing, orientation and high dip of the bedding joints, together with the remarkable height of the slope, induced to examine the stability of the slope against buckling, which could have been further favoured by the low basal and inter-layer shear strength provided by the clay infilling of bedding joints. The sharp undulation visible in the middle part of the bedding joint forming the failure surface suggests that the slab was formed by a 20 m thick pack of layers having a length and a width of approximately 60 m and 20 m, respectively. The buckled part of the pack of layers can be estimated to be some 40 m. Simple limit equilibrium analyses were performed both in static (Cavers, 1981) and dynamic (Shou and Wang, 2003) conditions. Peak shear strength of the basal joint was assumed with or without clay infilling, while the Young's modulus of the layers, being the mechanical parameter which mainly controls the phenomenon, was varied within the range of values provided by the 55-80 GSI interval (Table 4). The momentum of inertia was assumed as the sum of those of the single layers (Adam et al., 2022), whose average thickness measured in situ is 0.3 m. Horizontal seismic coefficient k_h was set equal to 0.23, while k_v was assumed as 0.5 k_h according to Sahoo et al. (2020). Analyses indicate that for a Young's modulus corresponding to a specific GSI value, the factor of safety against buckling (i.e., the ratio between the maximum axial load applicable to the bending part of slab and the driving force exerted by the slab uphill) is slightly higher than 1 in static conditions. Conversely, for the same value of Young's modulus, the factor of safety in dynamic conditions is lower than unity. These results suggest that buckling deformations could be ongoing at an early stage (see e.g., Wang et al., 2023) prior to October 30th 2016 failure, similar to those observed on the northern flank of the slope that still stands up (Figure 12). These deformations may have reduced strength along the basal failure surface, loosened the rock mass and increased layer fracturing. Consistently with the hypothesis of a buckling mechanism in the early deformation stage, it is worth noting that FEM analyses depict tensile failure after the October 26th event along the middle-upper part of the bedding joint J2. Moreover, it cannot be excluded that buckling failure may have been a concurring, destabilizing mechanism in the very final stage of the 2016 event.

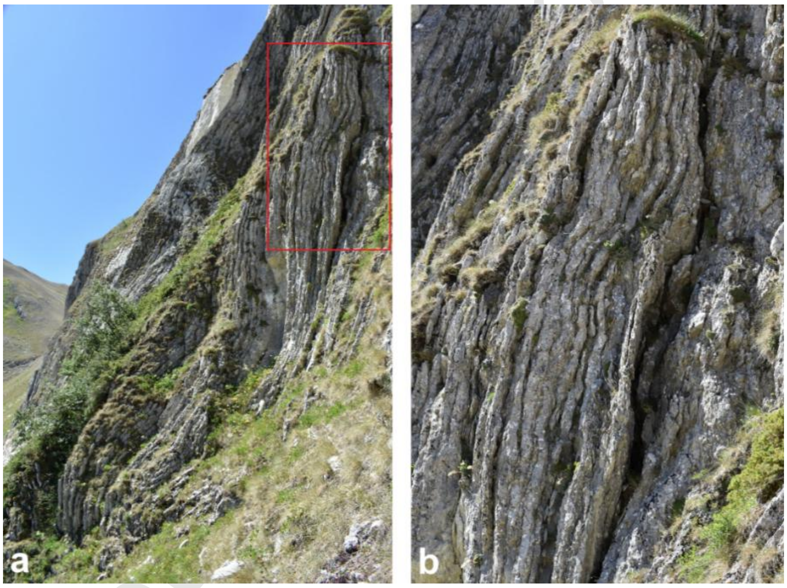

Figure 12: (a) folded strata on the northern flank of the investigated slope. The red box indicates the area enlarged in figure b; (b) example of early-stage flexural buckling affecting the strata.

However, despite the potential role of J2 in the failure process, static analysis indicates that rupture initially develops along J3 in the central sector of the slope and successively propagates both upslope and downslope along the other two discontinuities (Figure 7). This evolution differs from that obtained through dynamic analyses, where failure initiates along J1, in the upper part of the slope, and subsequently propagates downslope along J2 and eventually J3 (Figure 10). This difference can be explained by the distinct failure mechanisms expected in static and dynamic conditions, i.e., shear versus tensile failure.

Although the results of the dynamic analysis provided several insights into the timing and failure mechanisms of the Valle Orteccia rock slide, the analysis of total displacements and the distribution of points failed in tension (Figure 9-10) offered only a general overview of the phenomenon. In this regard, by comparing the displacement components along the three principal directions during both seismic events (Figure 13a-b), it is evident that the transverse displacement component (i.e., along the y-direction, perpendicular to the slope) is consistently and significantly more pronounced than the other two components.

In fact, the positive, transverse displacement-directed northward, where no lateral constraints are present, is only slightly lower than the total displacement and constitutes a distinctive feature of the failure mechanism. The predominance of leftward (northward) movement is further supported by the observed elongation of the blocky debris toward the left.

Analyzing the instantaneous displacements over time (Figure 13c), four main time-steps in the deformation process can be identified:

1. 3.2 s of the 26 October earthquake: an initial displacement peak is observed, with vectors predominantly oriented toward the N-NE direction;
2. 3.75 s of the 26 October earthquake: a second peak in displacement is recorded, but with a upward concavity, indicating a prevailing instantaneous movement approximately opposite to the previous one, i.e., toward the south. As already shown in Figure 8c, the combined effect of these two peaks results in widespread ruptures along discontinuities J1 and J2, and to a lesser extent, J3;
3. 1.2 s of the 30 October earthquake: in the early phase of this event, there is an apparent, slight reduction in total displacement, which can once again be explained by a dominant movement toward the negative Y-axis (i.e., southward);
4. 1.6 s of the 30 October earthquake: a large displacement peak occurs along the positive Y-axis, indicating substantial transverse movement toward the north. This movement triggers rupture at the intersection of discontinuities (Figure 10), marking the onset of the global failure process.

Regarding this latter stage, if we examine the relative shear stress τ_{rel} - defined as the ratio of mobilized shear stress to maximum shear strength - on the three main discontinuities (Figure 14), it is clear that the most critical conditions occur on J1 and J2. In contrast, J3 does not appear to play a significant role in shear resistance, suggesting that it mainly acts as a kinematic release surface for the event. Moreover, the concentration of areas with τ_{rel} =1 in the upper sections of J1 and J2 highlights how the upper part of the collapsed sector was more prone to fail. In turn, this suggests that the lower part may have become involved in the failure process only after the detachment of the upper sector.

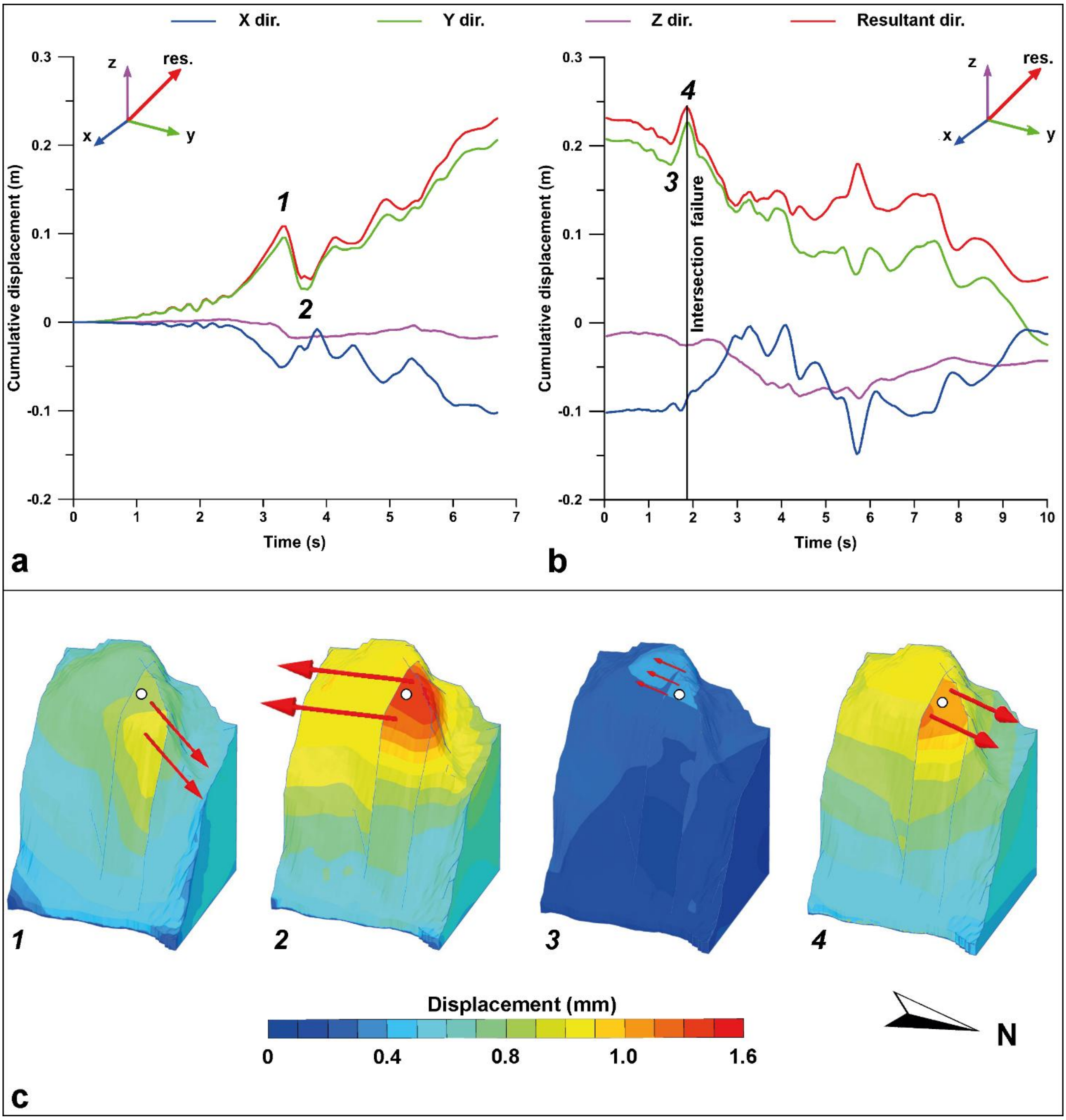

Figure 13: Time histories of the resultant and the components along the three axes (x, y, z) of the cumulative displacement calculated at the top-centre of the failed mass (white dot in Figure c) for the 26 October 2016 earthquake (a) and the 30 October 2016 earthquake (b). Spatial distribution of instantaneous displacements (c) at: 3.20 s (1) and 3.75 s (2) of Visso earthquake; 1.20 s (3) and 1.60 s (4) of Norcia earthquake. In all cases displacements concentrate within the upper part of the collapsed sector.

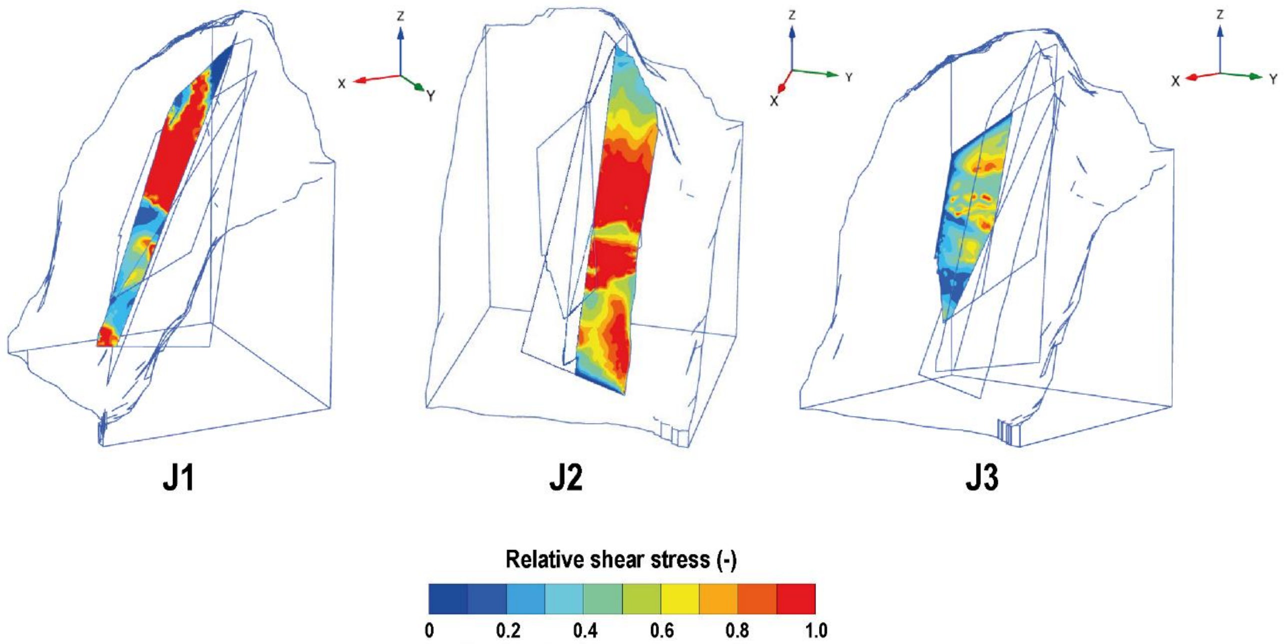

Figure 14: spatial distribution of relative shear stress τ_{rel} on the three main discontinuities at 1.6 s of the 30 October earthquake (onset of the global failure process).

The choice of seismic input motion plays a crucial role in numerical simulations of seismic response, as ground motion amplification strongly depends on both input motion characteristics and local ground conditions. While seismic hazard analyses typically rely on sets of acceleration time histories matched to a reference response spectrum (Pergalani et al., 2020), scenario reconstructions require input motions that closely resemble the actual earthquake affecting the study area. In this study, the seismic response of the Valle Orteccia slope is analysed aiming at modelling rock slide triggering during the 2016 Central Italy seismic sequence. The different response of various sectors of the slope to the seismic shaking was further investigated producing the spectrograms (Kanasewich, 1981 and references therein) of the horizontal components of the ground motion (x and y directions). These spectrograms, which illustrate the temporal evolution of the frequency content, show the different behavior of the basal (Figure 15a, 15d), lateral-upper (Figure 15b, 15e) and central-upper (Figure 15c, 15f) part of the slope. In the first two cases, the response is similar, with frequency content primarily concentrated in the 1-6 Hz range and peak energy observed between 3 and 5 s during the 26 October 2016 Visso earthquake, and between 3.5 and 6 s during the 30 October 2016 Norcia earthquake. By contrast, a more complex response characterizes the central part of the slope, corresponding to the collapsed sector. As shown in Figures 15c and 15f, the ground motion here covers a broader frequency range, extending up to 10 Hz for both seismic events. This variation reflects the complex, three-dimensional geometry of this slope portion, which likely induced waves focalization and amplification phenomena at different frequencies, enhancing the mobilization of sub-portions of the original slope.

The results of numerical modelling confirm the potential of a 3D analysis in achieving a more comprehensive and thorough reconstruction of the mechanisms leading to earthquake-induced rock slope failures, such as that occurred in Valle Orteccia. In particular, this analysis enables the reproduction of a complex failure mechanism, initially marked by significant horizontal displacements and a gradual release of the original kinematic constraints within the rock mass. This behavior, governed by the three-dimensional redistribution and reorganization of stresses and strains, cannot be adequately captured by other simplified approaches (Eroys and Kanik, 2025), such as limit equilibrium methods (Arslan Kelam et al., 2024).

From a geological-structural perspective, the relative position and orientation of the three main discontinuities played a key role in controlling the landslide geometry, while the steep slope morphology enhanced the amplification of the basal seismic input and, consequently, contributed to the failure initiation. This geological-structural setting is widespread across many areas of the central-northern Apennines, as it results from the contractional tectonic phase affecting the region. This phase led to the development of E-ENE-verging asymmetric folds with subvertical to overturned flanks, dissected by subvertical strike-slip faults along the entire orogenic belt (e.g., Pierantoni et al., 2013; Calamita et al., 2011; Curzi et al., 2024). Accordingly, we consider this sector particularly relevant for future studies aimed at identifying areas susceptible to earthquake-triggered landslides in the central-northern Apennines and in other fold-and-thrust belts with similar stratigraphic and tectonic settings.

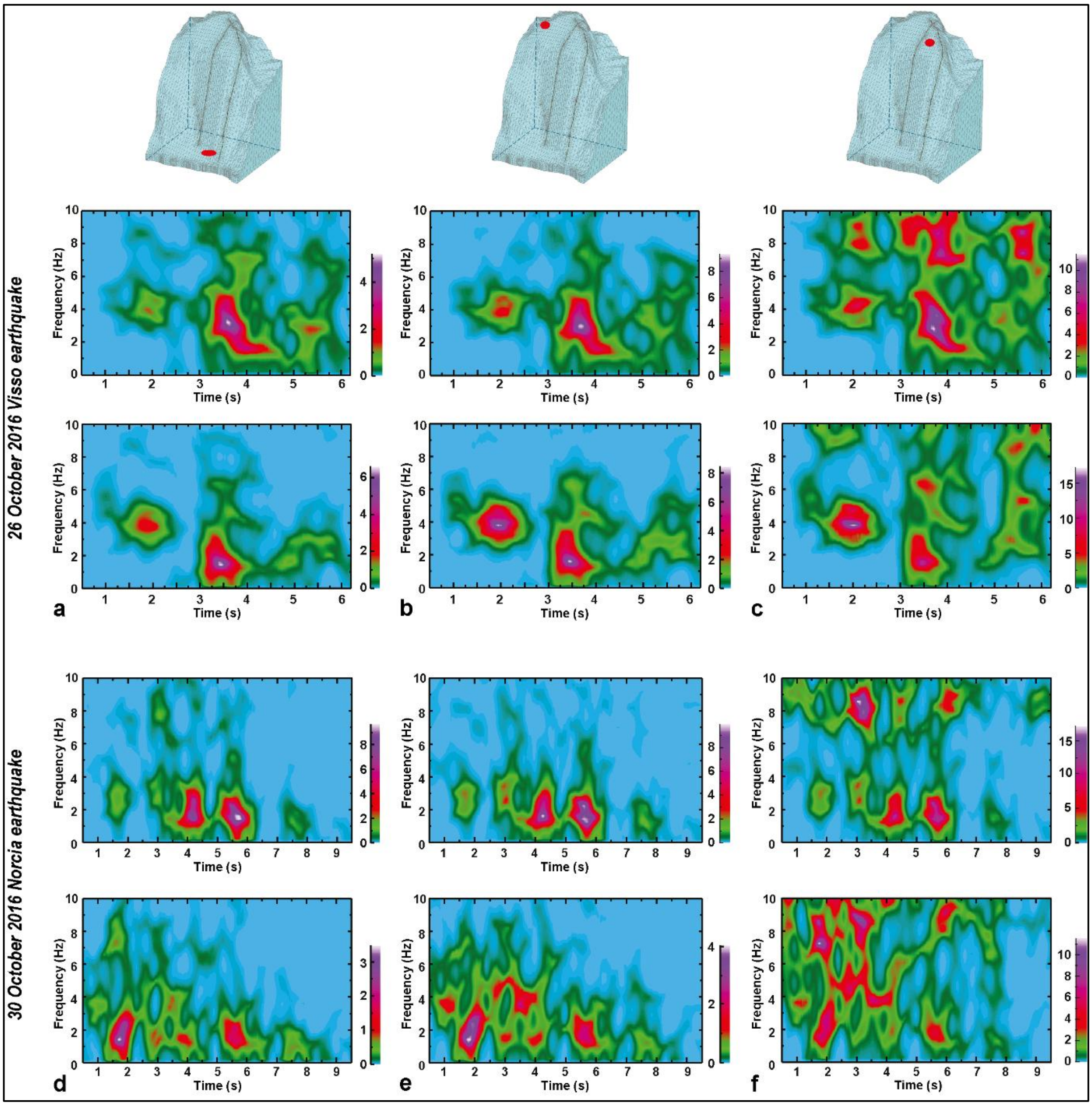

Figure 15: spectrograms of the horizontal components (x and y directions) of the ground motion at different locations of the slope during the 26 October 2016 earthquake and the 30 October 2016 earthquake. slope foot (a-d); lateral slope top (b-e); central slope top (c-f). The top figure refers to the x-direction, while the bottom one corresponds to the y-direction. The values shown in the legends should be multiplied by 10^{-3}.

6 Conclusions

In this work, we analyzed one of the main rock slope failures occurred during the 2016 Central Italy seismic sequence, i.e., the Valle Orteccia rock slide. The analysis of aerial/satellite images revealed that the slope survived the Mw5.9 October 26th 2016 Visso earthquake but failed after the Mw6.5 October 30th 2016 Norcia event.

To better understand the timing and mechanisms of the failure initiation, static and dynamic analyses, were conducted using with the FEM code Plaxis 3D, and based on reliable geological-structural and geomechanical data derived from UAV surveys and in-situ investigations. In particular the model included the major discontinuities, as they were highlighted by the landslide scar, and an anisotropic constitutive model that accounted for the regular bedding of the rock mass. Analyses indicate that, despite the slope initially exhibited a factor of safety 2.45, it reached a condition close to failure as early as the October 26th event and eventually failed during the first seconds of the October 30th event.

The progressive development of instability along the three very persistent discontinuities delimiting the failed volume was captured by the performed analyses, which also revealed that the highest displacement occurred along the y-direction (i.e., transverse to the slope), which likely triggered the full mobilization of the landslide mass. Dynamic analysis also indicated the important role of tensile rupture of rock bridges of discontinuities especially along the joints J2 and J1. This mechanism is in contrast to what observed in the static analysis, featured by prevailing shear failure over the bedding joint J2 and subordinately the J1 joint.

Ground accelerations highlight a significant modification of the seismic signal. The analysis pointed out clear amplification effects, almost twofold increasing in shaking amplitude, concentrated in the upper-central part of the slope, i.e., the collapsed sector, thereby emphasizing the role that a high, subvertical steep slope morphology had in the failure.

Despite some uncertainties mainly related to the mechanical parameter assigned to the different components of the rock mass, an analyses which combines the stress-strain approach, the actual 3d geometry of the slope and the representation of the main structural features of the rock mass enables a more accurate reconstruction of the development of displacements and distribution of points at yielding/tensile failure in both static and seismic conditions. In particular, the dynamic 3D modelling allows for a comprehensive an assessment of directional effects during the entire failure process, thus being much more realistic than a bi-dimensional approach.

Once again the structural setting of the rock mass proved to be fundamental in controlling failure mechanism, as already stressed by other Authors for the same seismic sequence and in the same area (eg., Franke et al., 2019) as well as in other seismological and geological contexts (e.g. Has and Nozaki, 2014). Nevertheless, the particular rock mass structure featuring the Valle Orteccia rock slide does not allow the use of simpler 3D analyses (i.e. limit equilibrium, both pseudostatic and dynamic) as effectively suggested for rock slides in the same area by Forte et al., 2021 and Verrucci et al., 2023. This is to be considered in a hazard assessment perspective, especially in interseismic conditions (as in the studied case), when the time due for the response could be too short compared to that required to set up the model and run a robust analysis.

The geological-structural setting of the Valle Orteccia site, which results from the tectonic evolution of the region and has proven to be particularly favorable to the triggering of earthquake-induced landslides. The geological–structural and morphological factors controlling this event are not site-specific but are representative of a broader class of earthquake-induced slope instabilities documented in orogenic areas that have undergone a comparable morpho-tectonic evolution. Consequently, the results of this study extend beyond the local scale and provide a robust basis for seismic slope stability analysis and hazard assessment in structurally complex mountainous environments.

Author contributions

Conceptualization: LSc, LSm, CV, PT, GF; Data curation: LSc, LSm, GF; Formal analysis: LSc, CV, PT; Investigation: LSc, LSm, PT, GF; Methodology: LSc, PT; Writing – original draft: LSc, LSm, CV, PT, GF; Writing – review and editing: LSc, LSm, CV, PT, GF.

Funding

This research has been supported by the Italian Ministry of Ecological Transition (Ministero della Transizione Ecologica) under the project FRA.SI – multi-scale integrated methodologies for seismically induced landslides hazard zonation in Italy (Metodologie integrate multi-scala per la zonazione della pericolosità da frana sismo-indotta in Italia) (grant no. bando DD 449/2018).

References

1. Adam, C., Ladurner, D., Furtmüller, T., 2022. Moderately large vibrations of flexibly bonded layered beams with initial imperfections. Composite Structures, 299, 116013. doi: 10.1016/j.compstruct.2022.116013.
2. Agliardi, F., Crosta, G.B., Meloni, F., Valle, C., Rivolta, C., 2013. Structurally-controlled instability, damage and slope failure in a porphyry rock mass. Tectonophysics, 605, 34-47. doi: 10.1016/j.tecto.2013.05.033.
3. Arslan Kelam, A., Akgün, H., Bobet, A., Koçkar, M.K., 2025. Assessment of Complex Rock Slope Instabilities in Mudurnu, Turkey, Through Kinematic and Dynamic Analyses: A Case Study. Rock Mech Rock Eng. 58, 2223–2242. https://doi.org/10.1007/s00603-024-04271-0
4. Atta, J., Bera, A.K., 2025. A comprehensive review of three-dimensional (3D) unreinforced slope stability: evolution and perspectives. European Journal of Environmental and Civil Engineering, 29, 2424-2447. doi: 10.1080/19648189.2025.2487045.
5. Aydin, A., Basu, A.,2005. The Schmidt hammer in rock material characterization. Engineering Geology. 81, 1-14. doi: 10.1016/j.enggeo.2005.06.006.
6. Azarafza, M., Koçkar, M.K., Faramarzi, L., 2021. Spacing and block volume estimation in discontinuous rock masses using image processing technique: a case study. Environ Earth Sci. 80, 471. doi:10.1007/s12665-021-09768-3
7. Bandis, S.C., 1990. Scale effects in the strength and deformability of rocks and rock joints. In: Proceedings of the 1st International Workshop on Scale Effects in Rock Masses, Loen, Norway, 7-8 June 1990: 59-76.
8. Barton, N., Bandis, S.C., 1982. Effect of block size on the shear behavior of jointed rocks. In: Proceedings of the 23rd Symposium on Rock Mechanics, Berkeley, CA, USA, 25-27 August 1982: pp. 739-760.
9. Bentley Systems Inc., 2022. Plaxis 3D-CONNECT Edition V22.01.
10. Calamita, F., Satolli, S., Scisciani, V., Esestime, P., Pace, P., 2011. Contrasting styles of fault reactivation in curved orogenic belts: Examples from the Central Apennines (Italy). Geological Society of America Bulletin. 123, 1097-1111. doi: 10.1130/B30276.1
11. Carminati, E., Lustrino, M., Cuffaro, M., Doglioni, C., 2010. Tectonics, magmatism and geodynamics of Italy: what we know and what we imagine. In: Beltrando M., Peccerillo A., Mattei M., Conticelli S., Doglioni C. (eds.) The Geology of Italy: tectonics and life along plate margins. Journal of the Virtual Explorer. 36, 9. doi:10.3809/jvirtex.2010.00226.
12. Cavers, D.S., 1981. Simple methods to analyze buckling of rock slopes. Rock Mechanics. 14, 87-104. doi: 10.1007/BF01239857.
13. CEN, 2004. Eurocode 8: design of structures for earthquake resistance—part 1: general rules, seismic actions and rules for buildings. European Committee for Standardization, Brussels
14. Chiarabba, C., Amato, A., Anselmi, M., Baccheschi, P., Bianchi, I., Cattaneo, M., Cecere, G., Chiaraluce, L., Ciaccio, M.G., De Gori, P., De Luca, G., Di Bona, M., Di Stefano, R., Faenza, L.,

Govoni, A., Improta, L., Lucente, F.P., Marchetti, A., Margheriti, L., Mele, F., Michelini, A., Monachesi, G., Moretti, M., Pastori, M., Piana Agostinetti, N., Piccinini, D., Roselli, P., Seccia, D., Valoroso, L. 2009. The 2009 L'Aquila (central Italy) Mw 6.3 earthquake: main shock and aftershocks. Geophysical Research Letters. 36, L18308. doi:10.1029/2009GL039627.

15. Chiaraluce, L., Di Stefano, R., Tinti, E., Scognamiglio, L., Michele, M., Casarotti, E., Cattaneo, M., De Gori, P., Chiarabba, C., Monachesi, G., Lombardi, A., Valoroso, L., Latorre, D., Marzorati, S., 2017. The 2016 central Italy seismic sequence: a first look at the mainshocks, aftershocks, and source models: Seismological Research Letters. 88, 757-771. doi: 10.1785/0220160221.
16. Curzi, M., Cipriani, A., Aldega, L., Billi, A., Carminati, E., Van der Lelij, R., Vignaroli, G., Viola, G., 2024. Architecture and permeability structure of the Sibillini Mts. Thrust and influence upon recent, extension-related seismicity in the central Apennines (Italy) through fault-valve behavior. Geological Society of America Bulletin.136, 3-26. doi: 10.1130/B36616.1.
17. Dai, Z., Wang, L., Zhang, K., Wang, L., Gao, X., 2022. Implementation of the Barton-Bandis nonlinear strength criterion into Mohr–Coulomb sliding failure model. Advances in Materials Science and Engineering. 1590884. doi: 10.1155/2022/1590884.
18. Dobry, R., Idriss, I.M., 1978. Duration characteristics of horizontal components of strong-motion earthquake records. Bulletin of the Seismological Society of America. 68, 1487-1520 doi: 10.1785/BSSA0680051487.
19. Elmo, D., Donati, D., Stead, D., 2018. Challenges in the characterisation of intact rock bridges in rock slopes. Engineering Geology. 245, 81-96. doi: 10.1016/j.enggeo.2018.06.014.
20. Ersoy, H., Kanik, M., 2025. The significance of utilizing 3D modeling to assess the impact of underground blasting on surface landslide stability. Engineering Geology. 354, 108211. doi:10.1016/j.enggeo.2025.108211.
21. Faccenna, C., Becker, T.W., Lucente, F.P., Jolivet, L., Rossetti, F., 2001. History of subduction and back-arc extension in the Central Mediterranean. Geophysical Journal International. 145, 809-820. doi: 10.1046/j.0956-540x.2001.01435.x.
22. Fan, W., Lv, J., Cao, Y., Shen, M., Deng, L., Wei, Y., 2019. Characteristics and block kinematics of a fault-related landslide in the Qinba Mountains, western China. Engineering Geology. 249, 162–171. doi: 10.1016/j.enggeo.2018.12.019
23. Firincioglu, B.S., Ercanoglu, M., 2021. Insights and perspectives into the limit equilibrium method from 2D and 3D analyses. Engineering Geology, 281, 105968. doi: 10.1016/j.enggeo.2020.105968.
24. Forte, G., Verrucci, L., Di Giulio, A., De Falco, M., Tommasi, P., Lanzo, G., Franke, K.W., Santo, A., 2021. Analysis of major rock slides that occurred during the 2016-2017 Central Italy seismic sequence. Engineering Geology. 290, 106194. doi: 10.1016/j.enggeo.2021.106194.
25. Gischig, V.S., Eberhardt, E., Moore, J.R., Hungr, O., 2015. On the seismic response of deep-seated rock slope instabilities-insights from numerical modelling. Engineering Geology. 193,1-18. doi: 10.1016/j.enggeo.2015.04.003
26. Görüm, T., Tanyas, H., Karabacak, F., Yılmaz, A., Girgin, S., Allstadt, K.E., Süzen, M.L, Burgi, P. 2023. Preliminary documentation of coseismic ground failure triggered by the February 6, 2023 Türkiye earthquake sequence. Engineering Geology. 327, 107315.
27. Graziani, A., Rotonda, T., Tommasi, P., 2009. Stability and deformation mode of a rock slide along interbeds reactivated by rainfall. Proceedings of the 1st Italian Workshop on Landslides, Naples, Italy, 8-10 June 2009, 1, 62-71. ISSN 9788889972182.
28. Has, B., Nozaki, T., 2014. Role of geological structure in the occurrence of earthquake-induced landslides, the case of the 2007 Mid-Niigata Offshore Earthquake, Japan , Engineering Geology, Volume 182, Part A, Pages 25-36.
29. Havenith, H.B., Vanini, M., Jongmans, D., Faccioli, E., 2003. Initiation of earthquake-induced slope failure: influence of topographical and other site specific amplification effects. Journal of Seismology. 7, 397-412. doi: 10.1023/A:1024534105559

30. Hoek, E., Brown, E.T., 1997. Practical estimates of rock mass strength. International Journal of Rock Mechanics and Mining Sciences, 34: 1165-1186. doi: 10.1016/S1365-1609(97)80069-X.
31. Hoek, E., Carranza-Torres, C., Corkum, B., 2002. Hoek-Brown failure criterion-2002 edition. Proceedings of NARMS-Tac 2002, 1: 267-273.
32. Hungr, O., Leroueil, S., Picarelli, L., 2014. The Varnes classification of landslide types, an update. Landslides, 11:167–194. doi : 10.1007/s10346-013-0436-y
33. Jaeger, J.C., 1960. Shear failure of anisotropic rocks. Geological Magazine. 97, 65-72. doi: 10.1017/S0016756800061100
34. Jennings, J.E., 1970. A mathematical theory for the calculation of the stability of slopes in open cast mines. Proceedings of the Symposium on the Theoretical Background to the Planning of Open Pit Mines, Johannesburg (South Africa). 87–102.
35. Kanasewich, E.R., 1981. Time sequence analysis in geophysics. The University of Alberta Press, Edmonton, Canada: 480 pp.
36. Kim, D.H., Gratchev, I., Balasubramaniam, A., 2013. Determination of joint roughness coefficient (JRC) for slope stability analysis: a case study from the Gold Coast area, Australia. Landslides. 10, 657-664. doi: 10.1007/s10346-013-0410-8.
37. Kocaman, S.; Çetinkaya, S.; Tunar, Ö.N.; Karakaş, G.; Karakaş, V.E., Gökçeoğlu, C., 2025. "Landslides triggered by the 6 February 2023 Kahramanmaraş earthquakes (Türkiye)," Turkish Journal of Earth Sciences. 34,1, 4. doi: 10.55730/1300-0985.1945
38. Krahn, J., Morgenstern, N.R., 1979. The ultimate frictional resistance of rock discontinuities. International Journal of Rock Mechanics and Mining Sciences & Geomechanics Abstracts, 16: 127-133, doi: 10.1016/0148-9062(79)91449-9.
39. Kumar, V., Himanshu, N., Burman, A., 2019. Rock slope analysis with nonlinear Hoek–Brown criterion incorporating equivalent Mohr–Coulomb parameters. Geotechnical and Geological Engineering, 37: 4741-4757. doi: 10.1007/s10706-019-00935-9
40. Lanzo, G., Tommasi, P., Ausilio, E., Aversa, S., Bozzoni, F., Cairo, R., d'Onofrio, A., Durante, M.G., Foti, S., Giallini, S., Mucciacciaro, M., Pagliaroli, A., Sica, S., Silvestri, F., Vessia, G., Zimmaro, P., 2019. Reconnaissance of geotechnical aspects of the 2016 Central Italy earthquakes, Bulletin of Earthquake Engineering, 17: 5495-5532. doi: 10.1007/s10518-018-0350-8.
41. Li, A.J., Merifeld, R.S., Lyamin, A.V., 2008. Stability charts for rock slopes based on the Hoek-Brown failure criterion. International Journal of Rock Mechanics and Mining Sciences, 45: 689-700. doi: 10.1016/j.ijrmms.2007.08.010
42. Li, H., Liu, Y., Liu, L., Xia, X., 2019. Numerical evaluation of topographic effects on seismic response of single-faced rock slopes. Bulletin of Engineering Geology and the Environment, 78: 1873-189. doi: 10.1007/s10064-017-1200-7.
43. Lin, H.D., Wang, W.C., Li, A.J. 2020. Investigation of dilatancy angle effects on slope stability using the 3D finite element method strength reduction technique. Computers and Geotechnics, 118: 103295. doi: 10.1016/j.compgeo.2019.103295.
44. Lowe, D.G., 2004. Distinctive image features from scale-invariant keypoints. International Journal of Computer Vision, 60: 91-110 doi: 10.1023/B:VISI.0000029664.99615.94.
45. Martino, S., Bozzano, F., Caporossi, P., D'angiò, D., Della Seta, M., Esposito, C., Fantini, A., Fiorucci, M., Giannini, L.M., Iannucci, R., Marmoni, G.M., Mazzanti, P., Missori, C., Moretto, S., Rivellino, S., Romeo, R.W., Sarandrea, P., Schilirò, L., Troiani, F., Varone, C., 2017. Ground effects triggered by the 24th August 2016, Mw 6.0 Amatrice (Italy) earthquake: surveys and inventoring to update the CEDIT catalogue. Geografia Fisica E Dinamica Quaternaria, 40: 77-95 doi: 10.4461/GFDQ.2017.40.7.
46. Martino, S., Bozzano, F., Caporossi, P., D'Angiò, D., Della Seta, M., Esposito, C., Fantini, A., Fiorucci, M., Giannini, L.M., Iannucci, R., Marmoni, G.M., Mazzanti, P., Missori, C., Moretto, S., Piacentini, D., Rivellino, S., Romeo, R.W., Sarandrea, P., Schilirò, L., Troiani, F., Varone, C.,

2019. Impact of landslides on transportation routes during the 2016–2017 Central Italy seismic sequence. Landslides, 16: 1221-1241 doi: 10.1007/s10346-019-01162-2.
47. McQuillan, A., Bar, N., 2023. The necessity of 3D analysis for open-pit rock slope stability studies: theory and practice. Journal of the Southern African Institute of Mining and Metallurgy. 123, 63-70. doi: 10.17159/24119717/2425/2023.
48. Pergalani, F., Pagliaroli, A., Bourdeau, C., Compagnoni, M., Lenti, L., Lualdi, M., Madiai, C., Martino, S., Razzano, R., Varone, C., Verrubbi, V., 2020.. Seismic microzoning map: approaches, results and applications after the 2016–2017 Central Italy seismic sequence. Bulletin of Earthquake Engineering, 18, 5595–5629. doi.10.1007/s10518-019-00640-1
49. Pierantoni, P., Deiana, G., Galdenzi, S., 2013. Stratigraphic and structural features of the Sibillini Mountains (Umbria-Marche Apennines, Italy). Italian Journal of Geosciences, 132: 497-520. doi: 10.3301/IJG.2013.08
50. Pignalosa, A., Forte, G., Budetta, P., Santo, A., 2022. Topographic amplification and debris remobilization as a cause for increasing rockfall hazard in seismic areas: a case study in Central Italy. Geomorphology, 403: 108160. doi: 10.1016/j.geomorph.2022.108160.
51. Porreca, M., Minelli, G., Ercoli, M., Brobia, A., Mancinelli, P., Cruciani, F., Giorgetti, C., Carboni, F., Mirabella, F., Cavinato, G., Cannata, A., Pauselli, C., Barchi, M.R., 2018. Seismic reflection profiles and subsurface geology of the area interested by the 2016–2017 earthquake sequence (Central Italy). Tectonics, 37: 1116-1137. doi: 10.1002/2017TC004915.
52. Romeo, S., Di Matteo, L., Melelli, L., Cencetti, C., Dragoni, W., Fredduzzi, A., 2017. Seismic-induced rockfalls and landslide dam following the October 30, 2016 earthquake in Central Italy. Landslides, 14: 1457-1465. doi: 10.1007/s10346-017-0841-8
53. Ruffolo, R.M., Shakoor, A., 2009. Variability of unconfined compressive strength in relation to number of test samples. Engineering Geology. 108, 16-23. doi: 10.1016/j.enggeo.2009.05.011.
54. Sahoo, P.P., Shukla, S.K., Ganesh, R., 2020. Taylor's slope stability chart for combined effects of horizontal and vertical seismic coefficients. Géotechnique, 70: 835-838. doi: 10.1680/jgeot.18.D.013.
55. Salvini, R., Vanneschi, C., Coggan, J.S., Mastrorocco, G., 2020. Evaluation of the use of UAV photogrammetry for rock discontinuity roughness characterization. Rock Mechanics and Rock Engineering, 53: 3699-3720. doi: 10.1007/s00603-020-02130-2.
56. Schilirò, L., Massaro, L., Forte, G., Santo, A., Tommasi, P., 2024. Analysis of earthquake-triggered landslides through an integrated Unmanned Aerial Vehicle-based approach: a case study from Central Italy. Remote Sensing, 16: 93. doi: 10.3390/rs16010093.
57. Semblat, J.F., Pecker, A., 2009. Waves and vibrations in soils: earthquakes, traffic, shocks, construction works. IUSS Press, Istituto Universitario di Studi Superiori di Pavia.
58. Shou, K.J., Wang, C.F., 2003. Analysis of the Chiufengershan landslide triggered by the 1999 Chi-Chi earthquake in Taiwan. Engineering Geology, 68: 237-250. doi: 10.1016/S0013-7952(02)00230-2.
59. Singh, B., Goel, R.K., 2011. Strength of discontinuities. In: Singh B., Goel R.K. (eds.) Engineering rock mass classification, Butterworth-Heinemann: 193-204. doi: 10.1016/B978-0-12-385878-8.00015-X.
60. Stelzer, M., 2015. Numerical Studies on the PLAXIS Jointed Rock Model. Master Thesis, TU Graz. Available at: https://diglib.tugraz.at/download.php?id=576a77cc111fa&location=browse (accessed on 26 August 2025).
61. Stucchi M., Meletti C., Montaldo V., Crowley H., Calvi G.M., Boschi E., 2011. Seismic Hazard Assessment (2003-2009) for the Italian Building Code. Bulletin of the Seismological Society of America, 101, 1885-1911. DOI: 10.1785/0120100130.
62. Testa, A., Boncio, P., Di Donato, M., Brozzetti, F., Cirillo, D., 2019. Mapping the geology of the 2016 Central Italy earthquake fault (Mt. Vettore – Mt. Bove fault, Sibillini Mts.): geological details on the Cupi-Ussita and Mt. Bove-Mt. Porche segments and overall pattern of coseismic surface faulting. Geological Field Trips, 11: 1-31. doi: 10.3301/GFT.2019.03.

63. Tommasi, P., Di Giulio, A., Santo, A., Forte, G., De Falco, M., Verrucci, L., Lanzo, G., Rotonda, T., Franke, K.W., 2019. Effects of the Central Italy 2016 seismic sequence on slope stability. In: Silvestri F., Moraci N. (eds.) Proceedings of 7th ICEGE Rome, Italy: 901-914, CRC Press, Leiden, ISBN 978-0-367-14328-2.
64. Verrucci, L., Forte, G., De Falco, M., Tommasi, P., Lanzo, G., Franke, K.W., Santo, A., 2023. Instantaneous limit equilibrium back analyses of major rockslides triggered during the 2016-2017 central Italy seismic sequence. Natural Hazards and Earth System Sciences, 23: 1177-1190. doi: 10.5194/nhess-23-1177-2023.
65. Wang, Q., Zhang, R., Zheng, H., Zhou, P., 2023. An analytical solution of critical sliding displacement for the flexural buckling failure of layered rock slopes. International Journal of Rock Mechanics and Mining Sciences, 169: 105450. doi: 10.1016/j.ijrmms.2023.105450.
66. Wang, W., Zhao, W., Chai, B., Du, J., Tang, L., Yi, X., 2022. Discontinuity interpretation and identification of potential rockfalls for high-steep slopes based on UAV nap-of-the-object photogrammetry. Computers and Geosciences. 166, 105191. doi: 10.1016/j.cageo.2022.105191.
67. Watman, A., Guccione, D.E., Thoeni, K., Giacomini, A., 2025. From rock mass to rockfall activity: A comprehensive rockfall assessment using 3D kinematic analysis and change detection. Engineering Geology, 359, 108437. doi:10.1016/j.enggeo.2025.108437.
68. Wu, Y., Wang, S., Carter, J.P., 2025. Three-dimensional dynamic analysis of seismic-induced rockslides and river blockage. Acta Geotechnica. 20, 6157–6179. doi: 10.1007/s11440-025-02772-y.
69. Zou, Y., Qi, S., Guo, S., Zheng, B., Zhan, Z., He, N., Huang, X., Hou, X., Liu, H., 2022. Factors controlling the spatial distribution of coseismic landslides triggered by the Mw 6.1 Ludian earthquake in China, Engineering Geology, 296: 106477. doi: 10.1016/j.enggeo.2021.106477.

Declaration of interests

☒The authors declare that they have no known competing financial interests or personal relationships that could have appeared to influence the work reported in this paper.

☐The authors declare the following financial interests/personal relationships which may be considered as potential competing interests:

Numerical analysis of the influence of 3D geometry and seismic input on rock-slope failures triggered by moderate to strong earthquakes: an example from the 2016 Central Italy seismic sequence

Luca Schilirò [1], Luca Smeraglia [1,2], Chiara Varone [1]*, Giovanni Forte [3], Paolo Tommasi [1]

[1] Istituto di Geologia Ambientale e Geoingegneria del Consiglio Nazionale delle Ricerche (CNR IGAG), Rome, Italy; luca.schiliro@cnr.it; luca.smeraglia@cnr.it; chiara.varone@cnr.it; paolo.tommasi@cnr.it

[2] Chrono- Environnement, Université Marie & Louis Pasteur, Besançon, France

[3] Dipartimento d'Ingegneria Civile, Edile e Ambientale, Università degli Studi di Napoli Federico II, Naples, Italy; giovanni.forte@unina.it

* corresponding author: Chiara Varone (chiara.varone@cnr.it)

Highlights

- A rock avalanche, triggered by the 2016 Central Italy seismic crisis, is studied.
- 3D static and dynamic high-resolution numerical simulations were performed.
- The combined effect of two earthquakes (M_w 5.9,M_w 6.5) leads to the slope collapse.
- Three discontinuities were fundamental in the triggering.

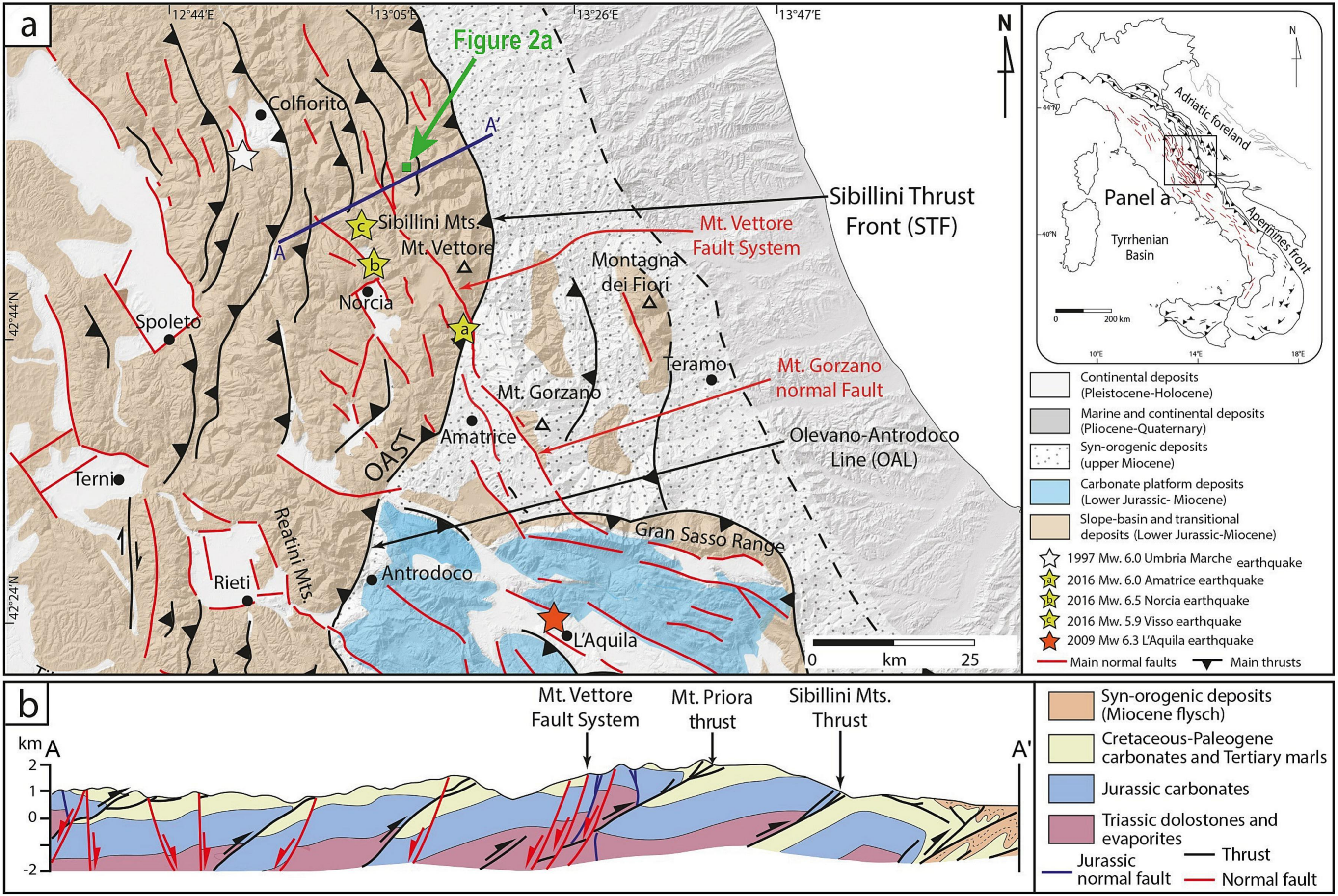

a
12°44'E
13°05'E
13°26'E
13°47'E
Figure 2a
N
Colfiorito
A'
A
Sibillini Mts.
Mt. Vettore
Norcia
Spoleto
Terni
Rieti
Reatini Mts.
Antrodoco
L'Aquila
OAST
Amatrice
Mt. Gorzano
Montagna dei Fiori
Teramo
Gran Sasso Range
42°44'N
42°24'N
Sibillini Thrust Front (STF)
Mt. Vettore Fault System
Mt. Gorzano normal Fault
Olevano-Antrodoco Line (OAL)
0 km 25
Adriatic foreland
Panel a
Tyrrhenian Basin
Apennines front
44°N
40°N
10°E
14°E
18°E
0 200 km
Continental deposits (Pleistocene-Holocene)
Marine and continental deposits (Pliocene-Quaternary)
Syn-orogenic deposits (upper Miocene)
Carbonate platform deposits (Lower Jurassic- Miocene)
Slope-basin and transitional deposits (Lower Jurassic-Miocene)
1997 Mw. 6.0 Umbria Marche earthquake
2016 Mw. 6.0 Amatrice earthquake
2016 Mw. 6.5 Norcia earthquake
2016 Mw. 5.9 Visso earthquake
2009 Mw 6.3 L'Aquila earthquake
Main normal faults
Main thrusts
b
Mt. Vettore Fault System
Mt. Priora thrust
Sibillini Mts. Thrust
km
A
A'
2
1
0
-2
Syn-orogenic deposits (Miocene flysch)
Cretaceous-Paleogene carbonates and Tertiary marls
Jurassic carbonates
Triassic dolostones and evaporites
Jurassic normal fault
Thrust
Normal fault

Figure 1

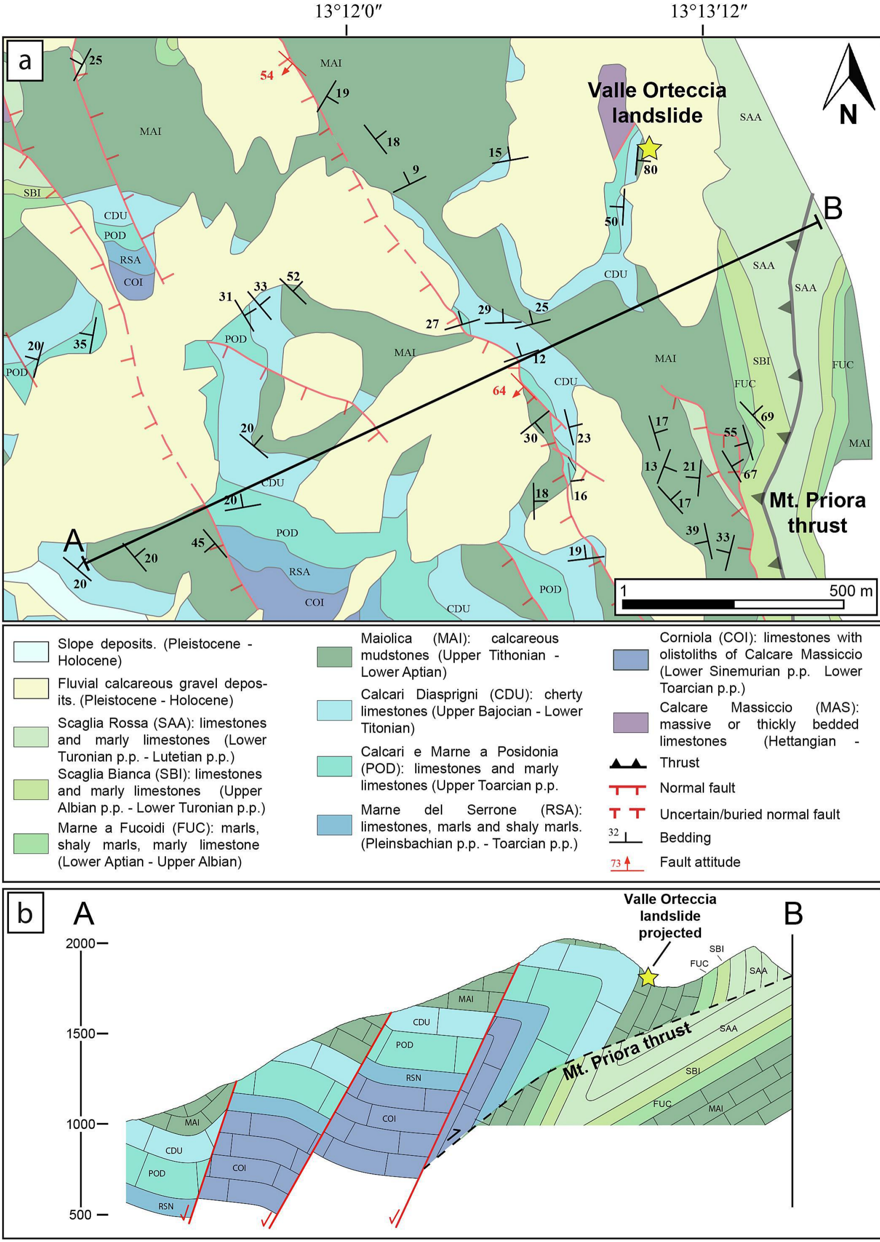
13°12′0″
13°13′12″
42°54′0″
a
Valle Orteccia landslide
N
Mt. Priora thrust
A
B
1
500 m
MAI
SAA
SBI
FUC
CDU
POD
RSA
COI
Slope deposits. (Pleistocene - Holocene)
Fluvial calcareous gravel deposits. (Pleistocene - Holocene)
Scaglia Rossa (SAA): limestones and marly limestones (Lower Turonian p.p. - Lutetian p.p.)
Scaglia Bianca (SBI): limestones and marly limestones (Upper Albian p.p. - Lower Turonian p.p.)
Marne a Fucoidi (FUC): marls, shaly marls, marly limestone (Lower Aptian - Upper Albian)
Maiolica (MAI): calcareous mudstones (Upper Tithonian - Lower Aptian)
Calcari Diasprigni (CDU): cherty limestones (Upper Bajocian - Lower Titonian)
Calcari e Marne a Posidonia (POD): limestones and marly limestones (Upper Toarcian p.p.
Marne del Serrone (RSA): limestones, marls and shaly marls. (Pleinsbachian p.p. - Toarcian p.p.)
Corniola (COI): limestones with olistoliths of Calcare Massiccio (Lower Sinemurian p.p. Lower Toarcian p.p.)
Calcare Massiccio (MAS): massive or thickly bedded limestones (Hettangian -
Thrust
Normal fault
Uncertain/buried normal fault
Bedding
Fault attitude
b
A
B
Valle Orteccia landslide projected
2000
1500
1000
500
Mt. Priora thrust
RSN

Figure 2

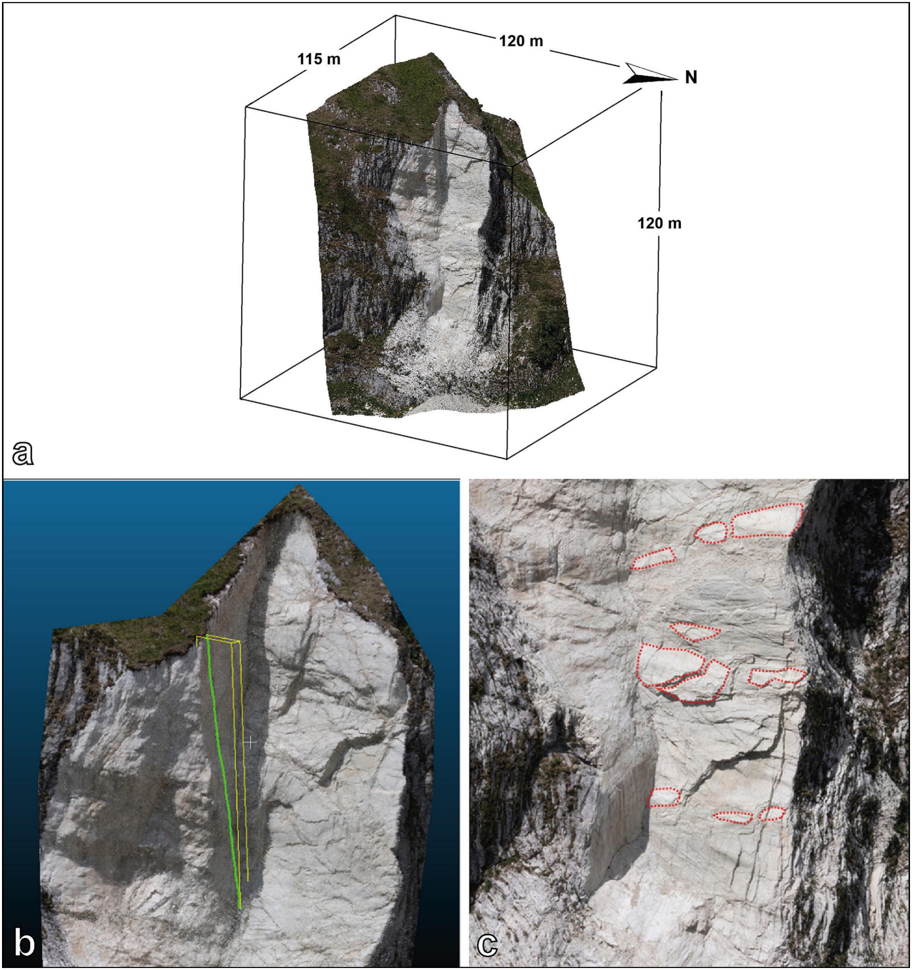

Figure 3

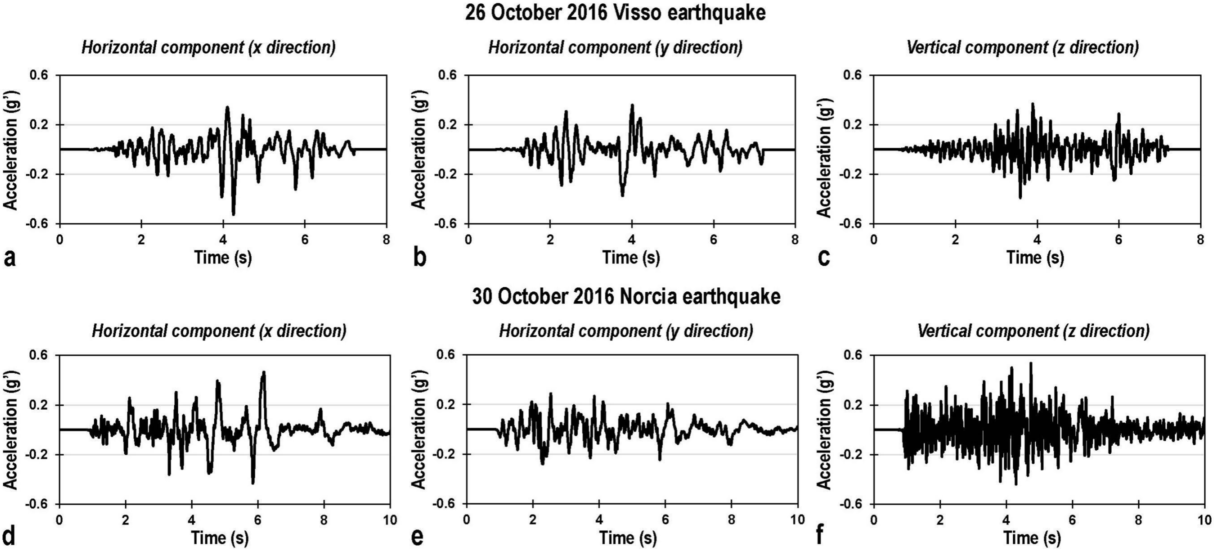
26 October 2016 Visso earthquake
Horizontal component (x direction)
Horizontal component (y direction)
Vertical component (z direction)
Acceleration (g')
Time (s)
a
b
c
30 October 2016 Norcia earthquake
Horizontal component (x direction)
Horizontal component (y direction)
Vertical component (z direction)
Acceleration (g')
Time (s)
d
e
f

Figure 4

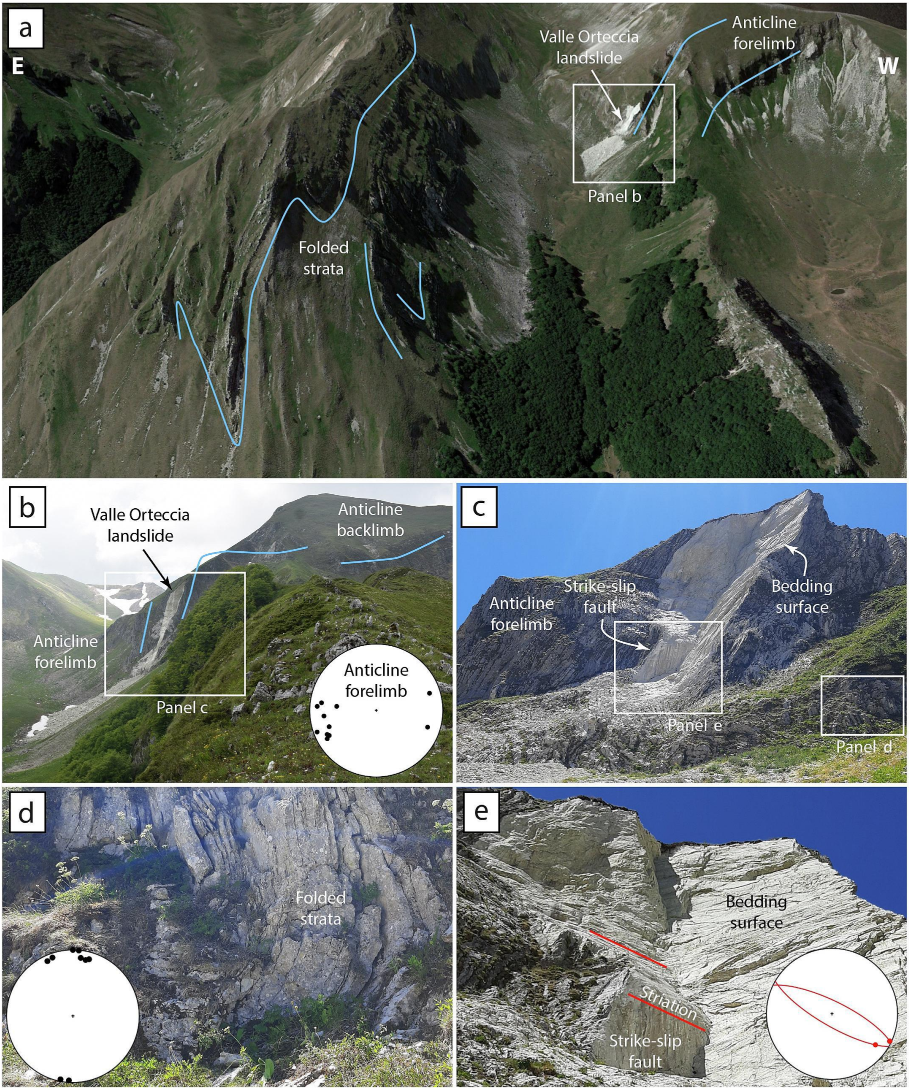

a
E
W
Valle Orteccia landslide
Anticline forelimb
Panel b
Folded strata
b
Valle Orteccia landslide
Anticline backlimb
Anticline forelimb
Panel c
Anticline forelimb
c
Strike-slip fault
Anticline forelimb
Bedding surface
Panel e
Panel d
d
Folded strata
e
Bedding surface
Striation
Strike-slip fault

Figure 5

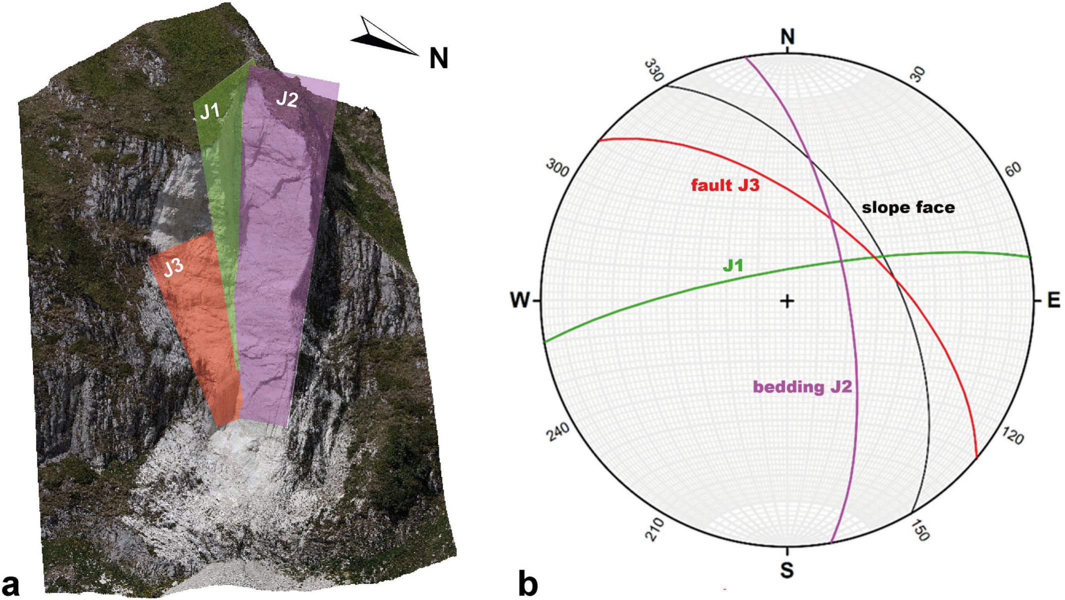

N
J1
J2
J3
a
N
330
30
300
60
fault J3
slope face
J1
W
E
bedding J2
240
120
210
150
S
b

Figure 6

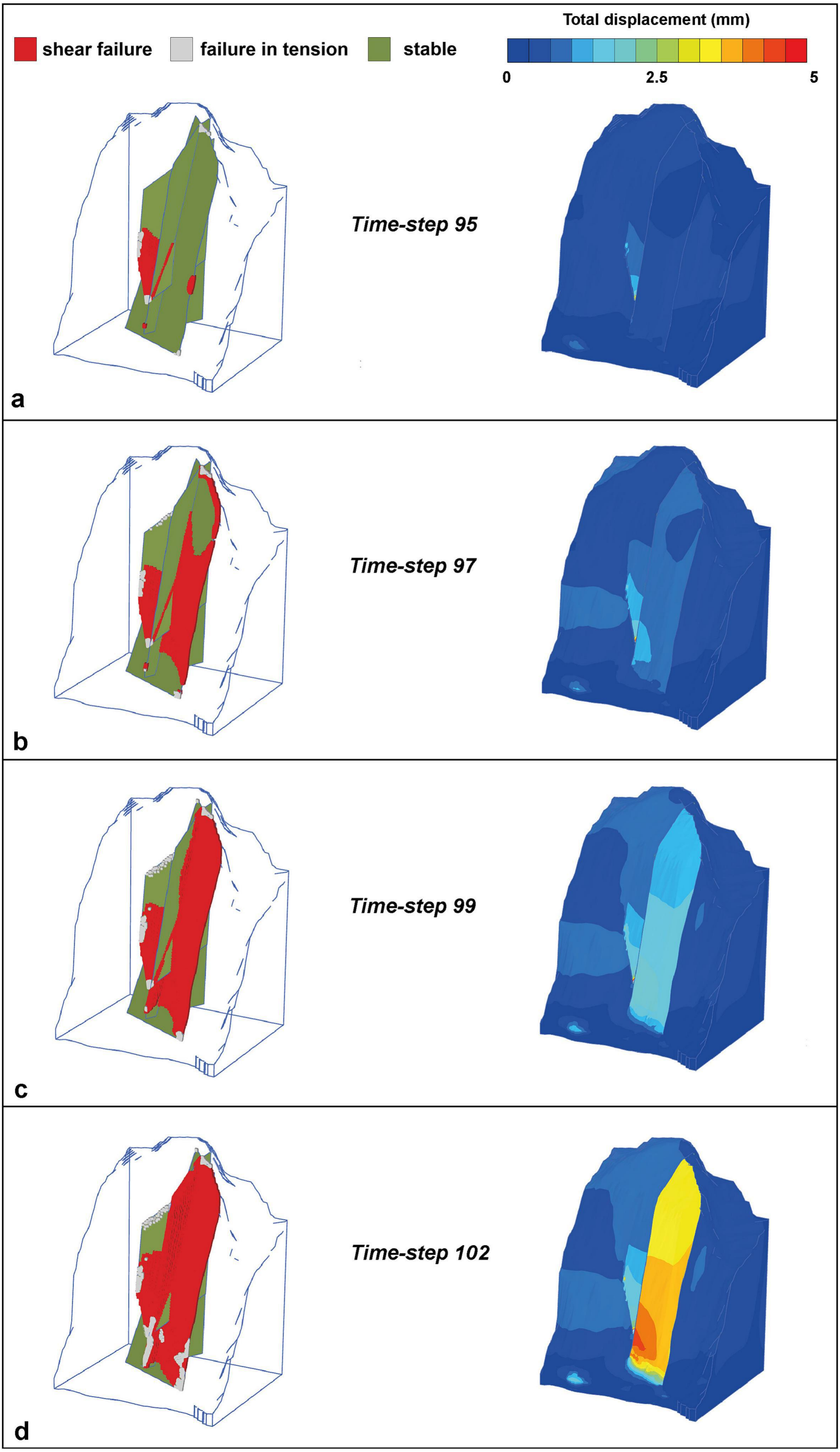
shear failure
failure in tension
stable
Total displacement (mm)
0
2.5
5
Time-step 95
a
Time-step 97
b
Time-step 99
c
Time-step 102
d

Figure 7

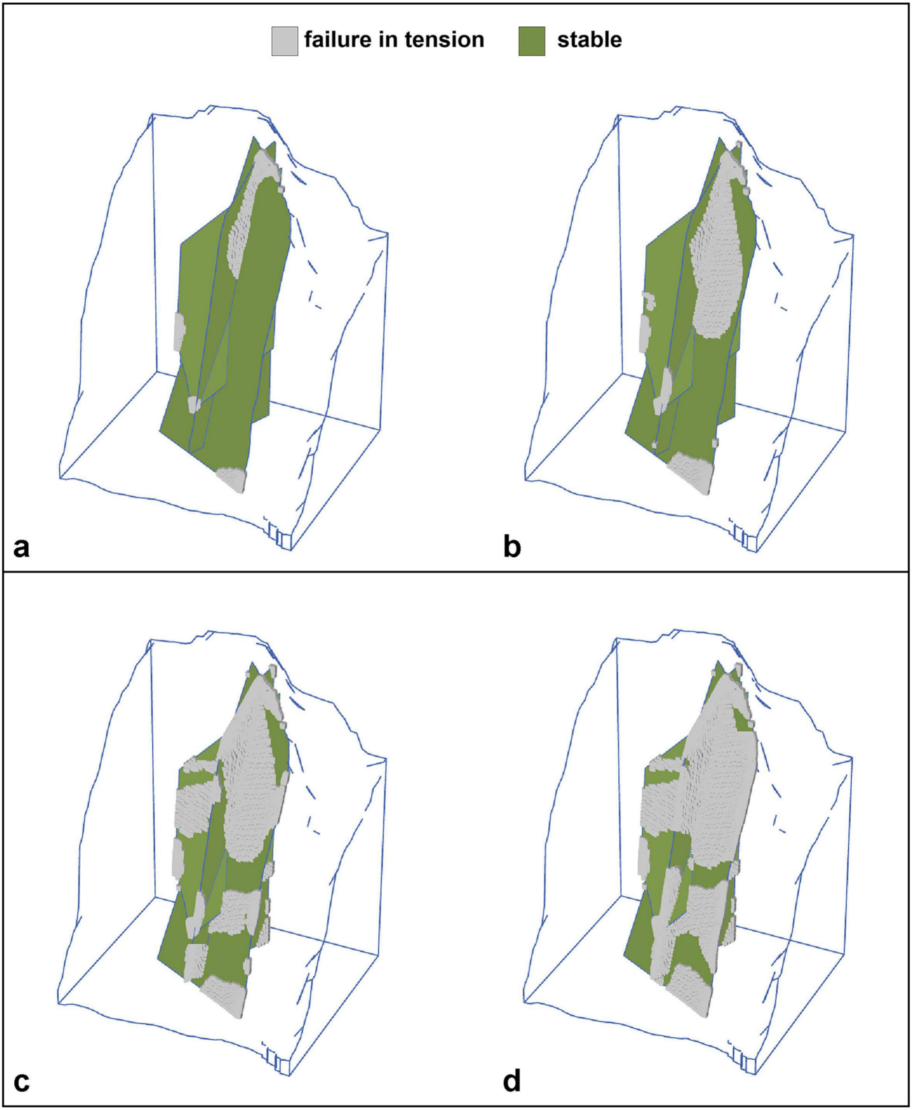

Figure 8

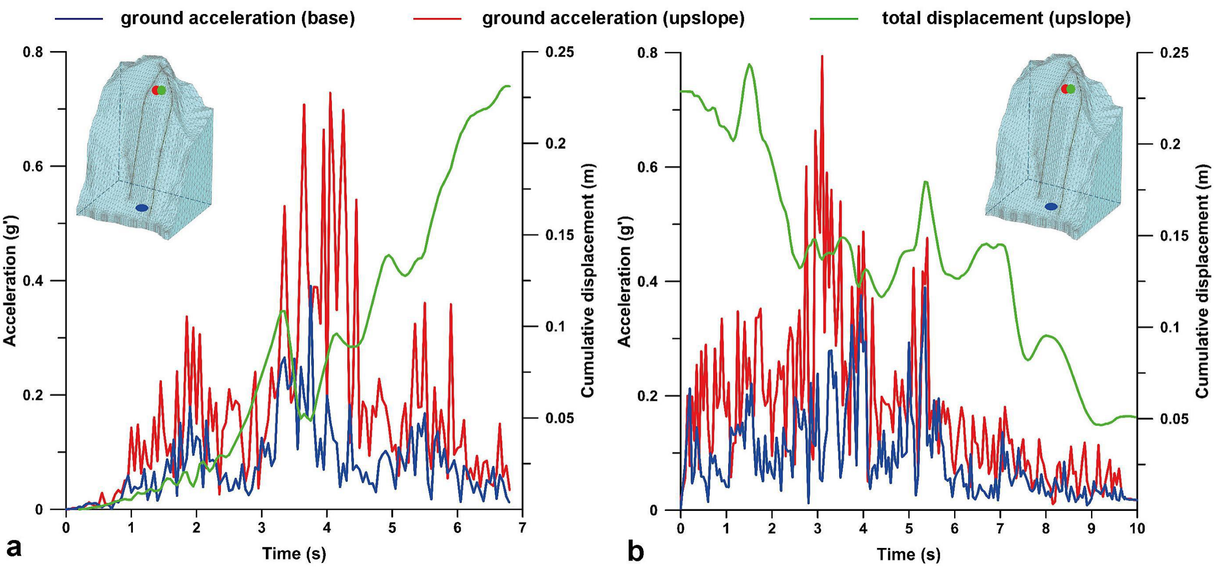

ground acceleration (base)
ground acceleration (upslope)
total displacement (upslope)
Acceleration (g')
Cumulative displacement (m)
Time (s)
a
b
0
0.2
0.4
0.6
0.8
0.05
0.1
0.15
0.2
0.25
0
1
2
3
4
5
6
7
8
9
10

Figure 9

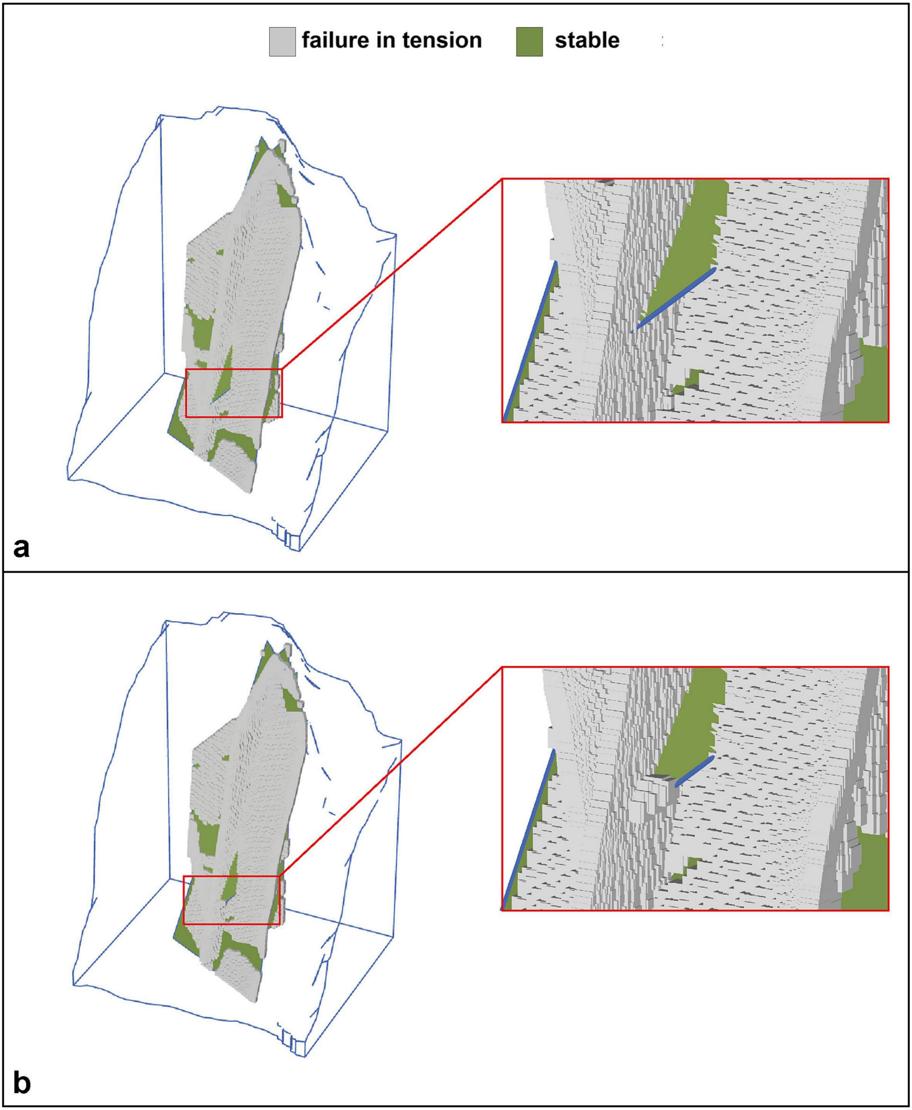

Figure 10

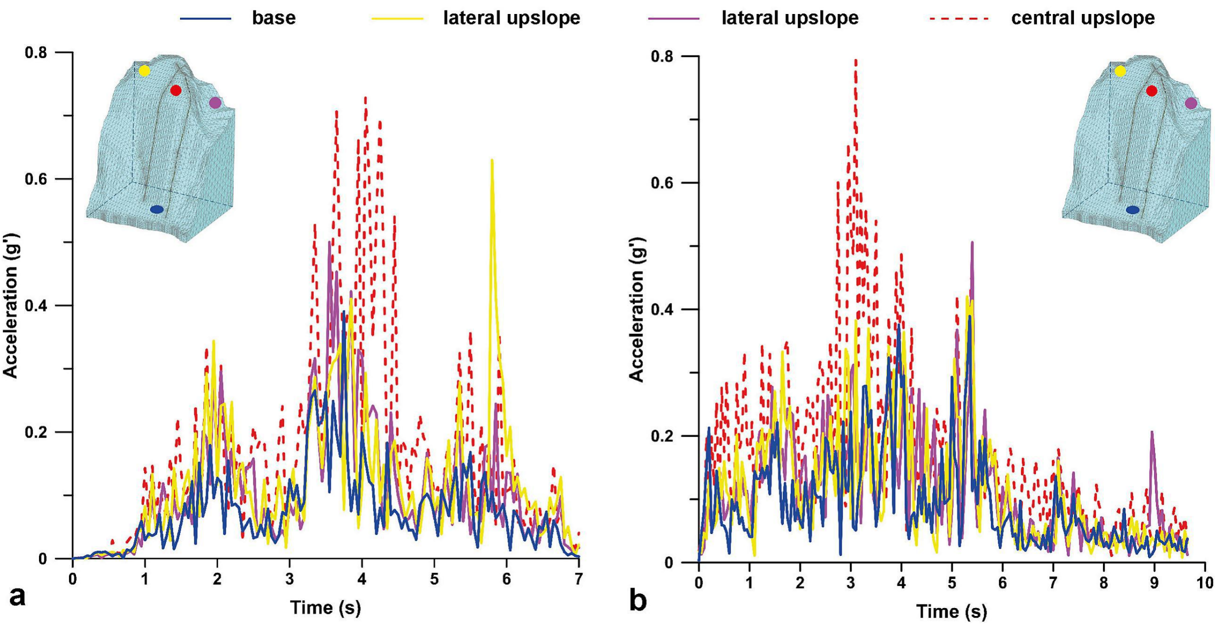

base
lateral upslope
lateral upslope
central upslope
Acceleration (g')
Time (s)
a
b
0
0.2
0.4
0.6
0.8
1
2
3
4
5
6
7
8
9
10

Figure 11

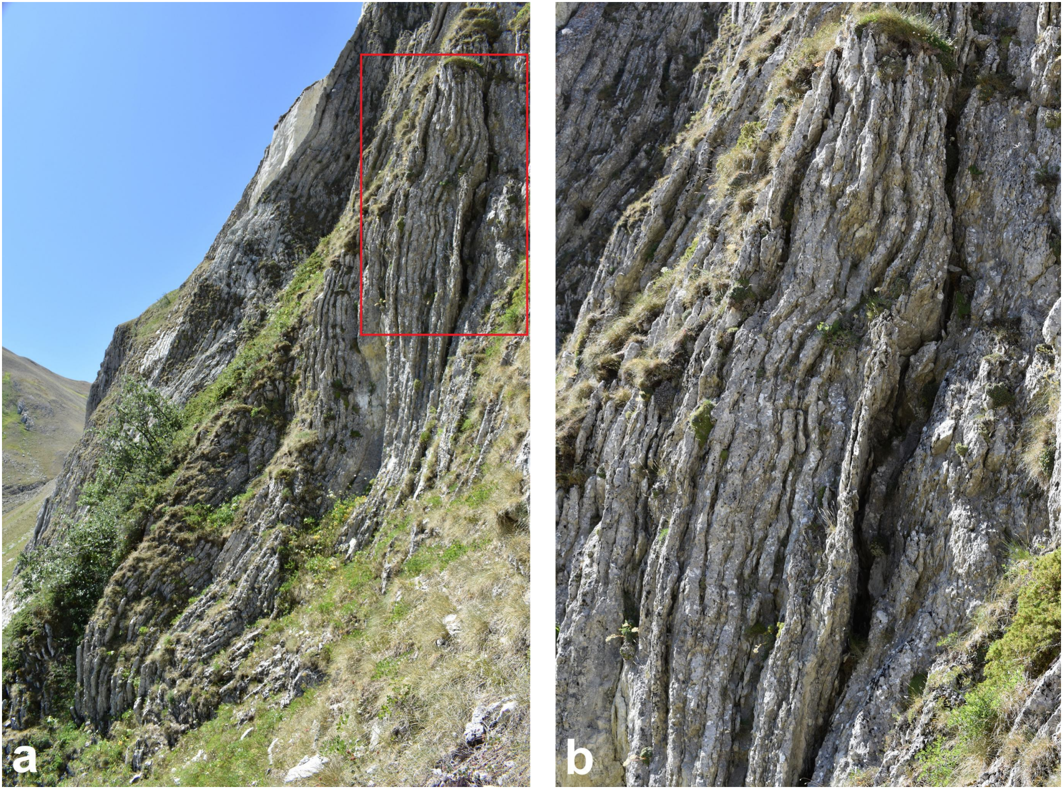

Figure 12

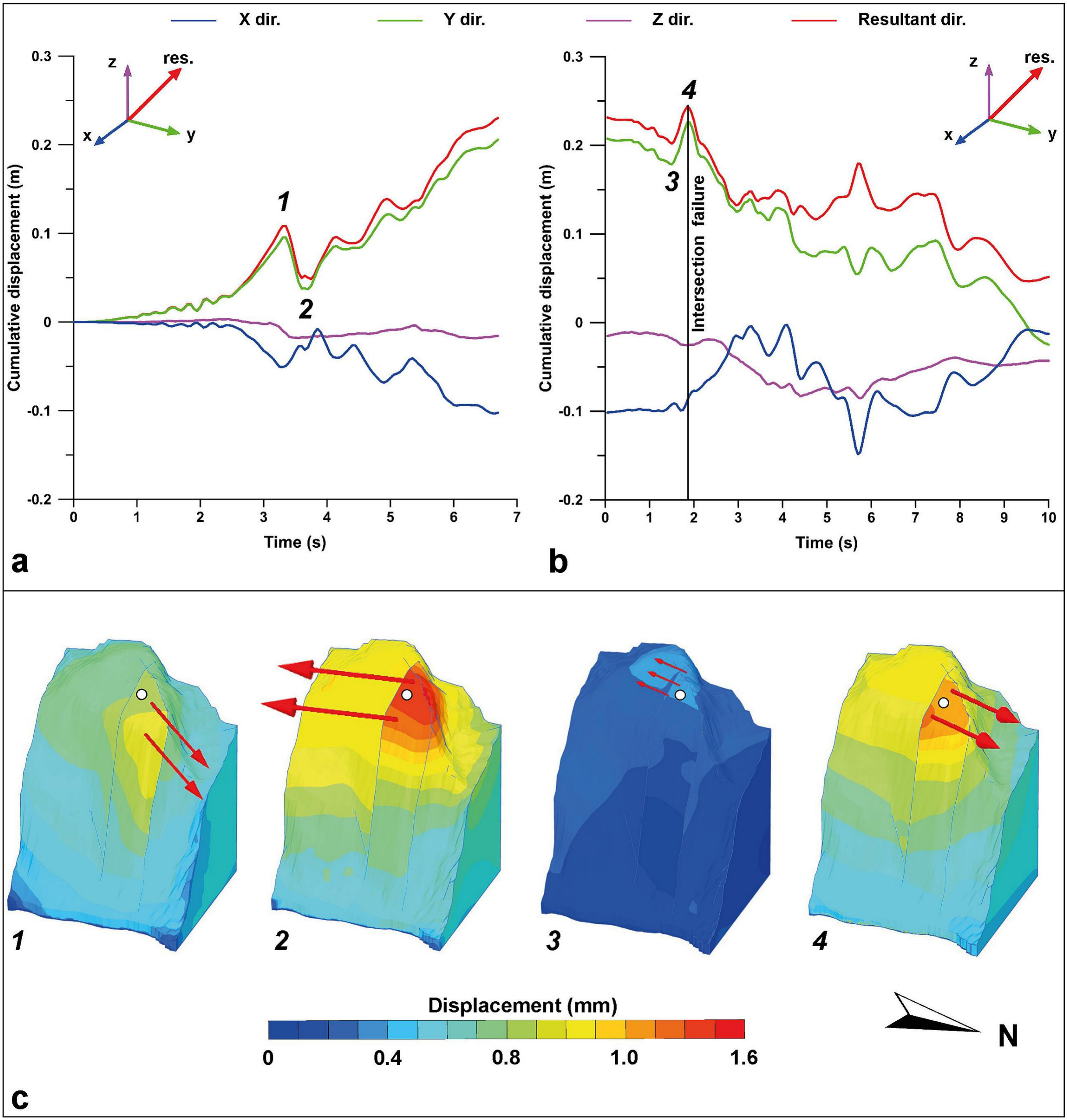
X dir.
Y dir.
Z dir.
Resultant dir.
z
res.
x
y
1
2
3
4
Intersection failure
Cumulative displacement (m)
Time (s)
0.3
0.2
0.1
0
-0.1
-0.2
0
1
2
3
4
5
6
7
8
9
10
a
b
c
Displacement (mm)
0
0.4
0.8
1.0
1.6
N

Figure 13

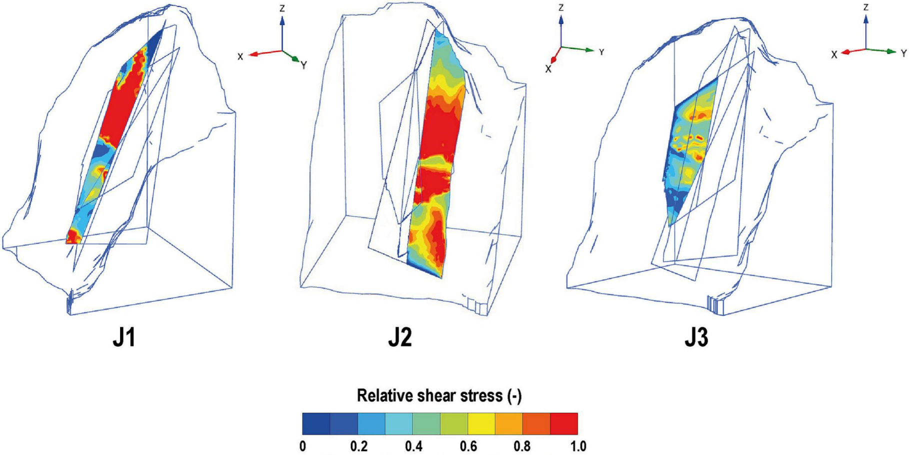

Figure 14

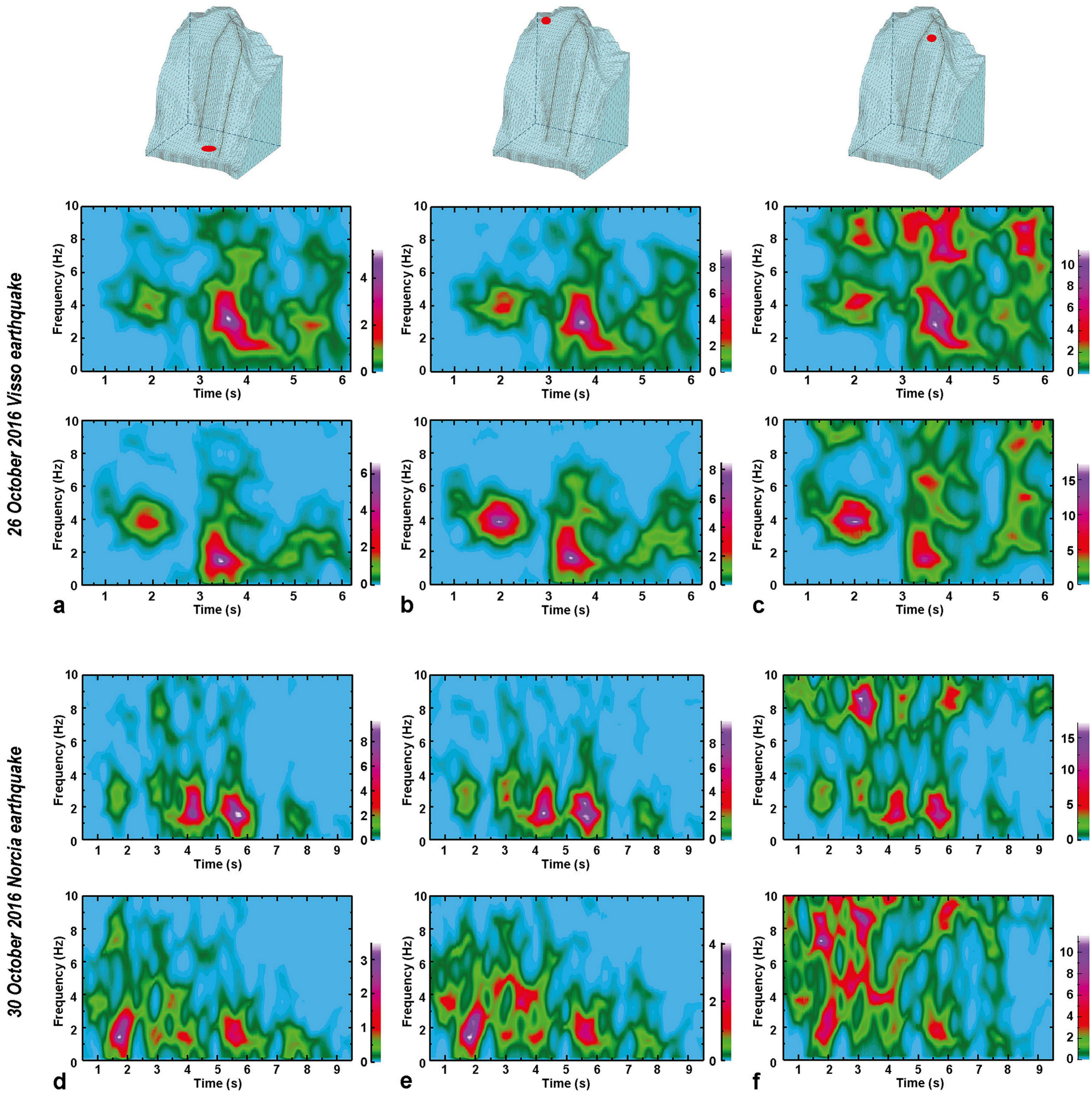
26 October 2016 Visso earthquake
30 October 2016 Norcia earthquake
Frequency (Hz)
Time (s)
a
b
c
d
e
f

Figure 15